Dynamic structural adaptations enable the endobiotic predation of *bdellovibrio bacteriovorus*

Mohammed Kaplan[1,#], Yi-Wei Chang[1,2,#], Catherine M. Oikonomou[1], William J. Nicolas[1], Andrew I. Jewett[3], Stefan Kreida[1,4], Przemysław Dutka[1,5], Lee A. Rettberg[1], Stefano Maggi[1]and Grant J. Jensen[1,6,*]

[1]Division of Biology and Biological Engineering, California Institute of Technology, Pasadena, CA 91125, USA

[2]Current address: Department of Biochemistry and Biophysics, Perelman School of Medicine, University of Pennsylvania, Philadelphia, PA 19104, USA

[3]Department of Integrative Structural and Computational Biology, The Scripps Research Institute, La Jolla, CA, USA

[4]Department of Microbiology, Tumor and Cell Biology, Karolinska Institute, 17177 Stockholm, Sweden

[5]Division od Chemistry and Chemical Engineering, California Institute of Technology, 1200 California Boulevard, Pasadena, CA 91125, USA

[6]Department of Chemistry and Biochemistry, Brigham Young University, Provo, UT 84604, USA

[*]Corresponding author: grant_jensen@byu.edu

[#]equal contribution

Graphical abstract

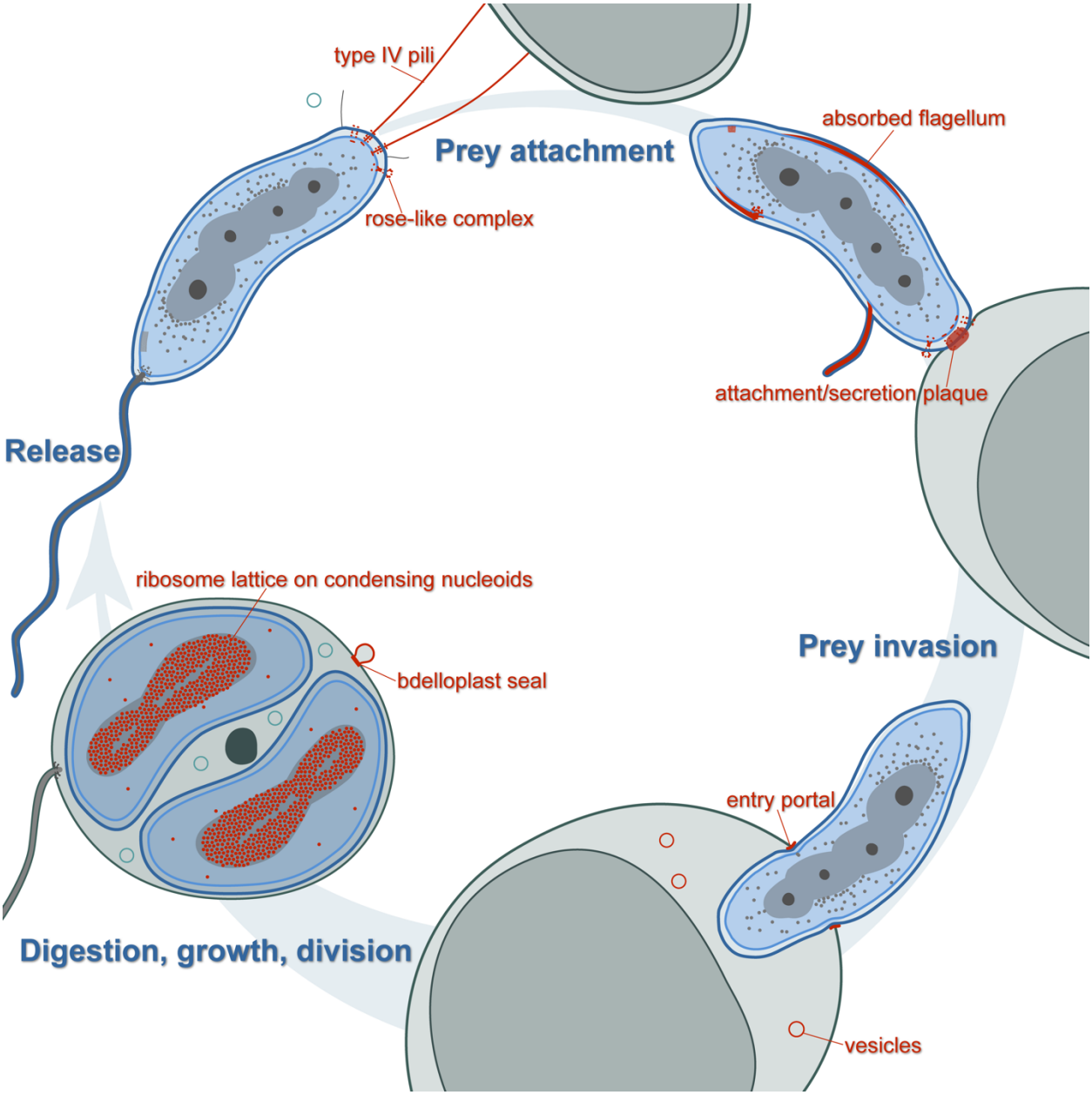

Abstract

Bdellovibrio bacteriovorus is an endobiotic microbial predator that offers promise as a living antibiotic for its ability to kill Gram-negative bacteria, including human pathogens. Even after six decades of study, fundamental details of its predation cycle remain mysterious. Here, we used cryo-electron tomography to comprehensively image the lifecycle of *B. bacteriovorus* at nanometer-scale resolution. In addition to providing the first high-resolution images of predation in a native (hydrated, unstained) state, we also discover several surprising features of the process, including novel macromolecular complexes involved in prey attachment/invasion and a flexible portal structure lining a hole in the prey peptidoglycan that tightly seals the prey outer membrane around the predator during entry. Unexpectedly, we find that *B. bacteriovorus* does not shed its flagellum during invasion, but rather resorbs it into its periplasm for degradation. Finally, following replication and division in the bdelloplast, we observe a transient and extensive ribosomal lattice on the condensed *B. bacteriovorus* nucleoid.

Introduction

Predation is a widespread behavior, from the largest eukaryotes to the smallest viruses, that drives evolution and energy flow in biological communities. In bacteria, predatory behavior is common and multiple predation types have been described, including epibiotic strategies in which the predator remains outside the prey and endobiotic strategies in which the predator invades the prey's cytoplasm or periplasm (Pérez et al., 2016). Since its description in 1963 as the first known bacterial parasite of bacteria (Stolp and Starr, 1963), *Bdellovibrio bacteriovorus* has been a paradigm of periplasmic endobiotic predation, in which a small predator takes up residence in a larger diderm prey's periplasm (Laloux, 2020; Sockett, 2009). The ability of *Bdellovibrio*-and-like-organisms (BALOs) to invade other Gram-negative bacteria, including human pathogens, has rendered them potential candidates for living antibiotics to tackle the crisis of antimicrobial resistance that has emerged in the past few decades (Bratanis et al., 2020; Cavallo et al., 2021; Harini et al., 2013; Iebba et al., 2014; Madhusoodanan, 2019; Negus et al., 2017; Pantanella et al., 2018; Raghunathan et al., 2019; Russo et al., 2018; Shatzkes et al., 2017a, 2017b), or even as a possible probiotic agent (Bonfiglio et al., 2020). For example, it has been shown that treating zebrafish infected with *Shigella flexneri* with *B. bacteriovorus* increases the animals' survival rate (Willis et al., 2016). In addition, microbial predation has been suggested to have been involved in pivotal evolutionary events including the genesis of eukaryotic cells, the rise of multicellularity, and pathogenicity (Davidov and Jurkevitch, 2009; Erken et al., 2013; Lyons and Kolter, 2015).

The predatory lifecycle of *B. bacteriovorus* has been extensively studied by methods including conventional transmission electron microscopy, light/fluorescence microscopy, helium-ion microscopy, atomic force microscopy and biochemical assays (Burnham et al., 1968; Kuru et al.,

2017; Makowski et al., 2020; Núñez et al., 2003; Said et al., 2019; Stolp and Starr, 1965), and is the subject of several excellent reviews (see for example: (Cavallo et al., 2021; Laloux, 2020; Negus et al., 2017; Rotem et al., 2014; Sockett, 2009)). In the free-living attack phase, the predator is transcriptionally streamlined, with a highly compacted spiral nucleoid (Butan et al., 2011), and a vibrioid cell shape caused by the asymmetric activity of a peptidoglycan hydrolase (Banks et al., 2022). At one pole of the cell, a sheathed unipolar flagellum enables high-velocity (up to 160 μm/s (Lambert et al., 2006; Rendulic, 2004)) motile collisions with prey. The flagellar filament has a distinctive damped waveform due to segments made up of subunits with different helical properties (Thomashow and Rittenberg, 1985a). Initial interaction with, and attachment to, prey is mediated by type IVb (Avidan et al., 2017) and type IVa pili (T4P) (Evans et al., 2007; Mahmoud and Koval, 2010; Milner et al., 2014) at the pole opposite the flagellum (the "biting pole"). Following this initial interaction, *B. bacteriovorus* uses flagellum-independent gliding motility to reach an attachment site on the side of rod-shaped prey cells (Lambert et al., 2011).

Upon initial attachment, prey quality is assessed in a cyclic-di-GMP-dependent process (Caulton and Lovering, 2020; Hobley et al., 2012; Meek et al., 2019), and if the prey is found to be suitable and not already under attack by another predator (Lerner et al., 2012), the attachment is made permanent and the process of invasion begins. Initially, it was suggested that a "drilling" mechanism caused by flagellar rotation might play a role in the invasion process (Burnham et al., 1968; Stolp and Starr, 1965), but later studies found that flagellar motility-compromised mutants can still invade prey, which fits with the roles of pili and gliding motility mentioned above (Lambert et al., 2006). Another early penetration model hypothesized that entry is passive and

occurs due to osmotic forces from the flux of solutes and water resulting from structural changes in the prey envelope (Abram et al., 1974).

Prey invasion involves enzymatic modification of the prey cell wall by *B. bacteriovorus* at the predator-prey contact point (Kuru et al., 2017; Thomashow and Rittenberg, 1978c, 1978b, 1978a; Tudor et al., 1990) and is associated with the secretion, by type I and II secretion systems, of many enzymes (Pasternak et al., 2014; Rendulic, 2004), including glycanases (Harding et al., 2020; Thomashow and Rittenberg, 1978a), peptidases (Lerner et al., 2012; Tudor et al., 1990) and deacetylases (Lambert et al., 2016). A self-protection protein in *B. bacteriovorus* inhibits the predator's peptidases, thereby allowing specific modification of the prey cell wall (Lambert et al., 2015). These modifications round the prey cell and greatly expand the periplasmic space, providing room for the predator to enter. Entry itself is rapid, occurring in a few minutes or less (Abram et al., 1974; Capeness et al., 2013). With a few exceptions noted (Iida et al., 2009; Lambert et al., 2006), flagella are no longer visible on *B. bacteriovorus* when they enter their prey (Shilo, 1969; Thomashow, L. S., 1979).

Once *B. bacteriovorus* enters the prey's periplasm, the entry pore is sealed and transpeptidases modify the prey cell wall to render it more robust to osmotic pressure (Kuru et al., 2017; Lerner et al., 2012), forming what is known as the bdelloplast (Starr and Baigent, 1966). If prey-derived cues indicate the availability of sufficient nutrients in the bdelloplast (Rotem et al., 2015), *B. bacteriovorus* enters its growth phase. The predator consumes the cytoplasmic contents of the prey, facilitated by translocation of outer membrane (OM) pore proteins into the prey's cytoplasmic membrane (Tudor and Karp, 1994) and secretion of nucleases to digest the prey's nucleic acids

(Bukowska-Faniband et al., 2020). This fuels predator growth, through bidirectional elongation, and replication of its genetic material (Makowski et al., 2019). Once available nutrients are exhausted, the predator septates synchronously into multiple progeny cells by non-binary fission, with the number of progeny cells depending on the size of the prey (Fenton et al., 2010a; Kaljević et al., 2021). Finally, the progeny cells, reset to the attack phase, use an enzyme specific for deacetylated peptidoglycan to lyse the prey cell wall (Harding et al., 2020; Lambert et al., 2016), creating pores through which they exit the bdelloplast and move on in search of new prey (Fenton et al., 2010a). If the first invasion does not yield sufficient nutrients for replication and division, a *B. bacteriovorus* cell may leave the first bdelloplast and complete its lifecycle in a second prey (Makowski et al., 2019).

Despite extensive study, the structural details of much of the invasion process remain unclear. Most of the previous work relied on low-resolution imaging methods or conventional electron microscopy preparations, in which dehydration and fixation disrupt cell membranes and obscure macromolecular details. Cryogenic electron tomography (cryo-ET) allows the investigation of cellular processes in a fully-hydrated frozen state with macromolecular resolution (Ghosal et al., 2019a; Kaplan et al., 2021a; Oikonomou and Jensen, 2017), but so far it has only been applied to study the ultrastructure of individual *B. bacteriovorus* cells in the attack phase. While these studies revealed important structural features of this stage (Borgnia et al., 2008; Butan et al., 2011; Fenton et al., 2010b), much remains to be learned about the full invasion cycle of *B. bacteriovorus*.

Here, we used cryo-ET to image the predation cycle of *B. bacteriovorus* invading three types of prey: *Vibrio cholerae, Escherichia coli*, and *E. coli* minicells. Our work reveals, for the first time,

136 the macromolecular details of each stage of the *B. bacteriovorus* lifecycle and uncovers several
137 unexpected features of the process, including absorption of the extracellular flagellum into the
138 predator's periplasm during attachment, a flexible portal structure associated with the prey
139 peptidoglycan surrounding the predator during entry, and formation of a ribosome lattice around
140 the predator's nucleoid after the prey is consumed in the bdelloplast.
141
142

Results

To visualize the predatory lifecycle of *B. bacteriovorus* in a near-native state, we applied cryo-ET imaging to samples of *B. bacteriovorus* HD100 at various timepoints, from 10 minutes to 16 hours, after addition of prey (*Vibrio cholerae*, *Escherichia coli*, or *E. coli* minicells). Compared to thicker cells, the thinness of *E. coli* minicells yielded higher-resolution details about the predator-prey interaction. The small size of the minicells also prevented complete entry of the predator, allowing us to capture otherwise fleeting intermediates in the rapid invasion process. Table S1 lists the number of cryo-tomograms we acquired at each stage of the predatory lifecycle of *B. bacteriovorus*, and Table S2 the number of examples we observed of each of the features described below.

I- Anatomy of the attack-phase *B. bacteriovorus* cell

Our cryo-tomograms of attack-phase *B. bacteriovorus* showed features previously described, including a compact spiral nucleoid occupying the center of the cell (Fig. 1A) (Borgnia et al., 2008; Butan et al., 2011). While the nucleoid excluded ribosomes, they were occasionally abundant at its periphery (Fig. S1 and Movie S1), as seen previously by cryo-ET (Borgnia et al., 2008; Butan et al., 2011). Again consistent with previous cryo-ET of attack-phase cells (Borgnia et al., 2008), we saw unidentified tubes (on average, two per cell) in the cytoplasm. The tubes had a uniform diameter of ~8 nm and were typically a few tens of nanometers in length (Fig. S2). Each cell contained a single polar flagellum, sheathed in outer membrane (Fig. 1A), and subtomogram averaging of 79 particles revealed that the structure of the flagellar motor is similar to that recently published from a host-independent strain of *B. bacteriovorus* (Chaban et al., 2018) (Fig. 1B).

We also saw novel features, including extracellular vesicles with a uniform diameter of ~25 nm near cells (Fig. S3A). On the "biting" pole opposite the flagellum, we noted several characteristic features that have not been described before. Rarely, we saw spherical and short filamentous structures in the periplasm (Figs. 1A and S3B). We observed abundant, thin (~3-4 nm wide) fimbriae on the cell surface, with lengths ranging from ~50 to more than 100 nm (Fig. S3A&C). We also observed a novel complex, spanning the periplasm and with a prominent extracellular rosette of density. We call this unidentified structure the "rose-like complex." On average, each cell had 2-3 rose-like complexes at the biting pole (Fig. 1A). Subtomogram averaging of 132 particles revealed a molecular complex spanning the entire periplasmic space with associated cytoplasmic densities (a ring ~17 nm in diameter) and extensive extracellular densities. Five distinct extracellular densities could be distinguished in cross-section: two stacked rings and a central cap (Fig. 1C).

We observed both piliated and non-piliated T4aP basal bodies on the biting pole (Figs. 1A and S4 and S5), with empty more abundant than piliated (Table S2). A subtomogram average of 335 non-piliated T4aP basal bodies revealed the architecture, including a distinctive extracellular ring present in both non-piliated and piliated basal bodies (Figs. 1D and S4) which was not seen in subtomogram averages of T4P in other species (Chang et al., 2016, 2017; Gold et al., 2015; Treuner-Lange et al., 2020). While all piliated basal bodies had the ring, not all non-piliated basal bodies did (Fig. S5). This could either be because the external ring had disassembled or not yet assembled, or because these structures were not in fact T4aP but rather, e.g. T4bP, which are also involved in adhesion to prey (Avidan et al., 2017). In addition, classifying the non-piliated T4aP using principal component analysis revealed that ~1/2 of the particles had only the Secretin outer

188 membrane channel and extracellular ring and lacked the lower periplasmic ring (Fig. S6). This
189 might reflect different assembly stages, as it has been shown that T4P in other species utilize an
190 outside-in assembly pathway starting from the Secretin (Friedrich et al., 2014).
191
192 **II- Attachment of *B. bacteriovorus* to prey**
193 We observed attachment of *B. bacteriovorus* to *V. cholerae* and *E. coli* minicells (of various sizes).
194 The earliest event we identified was connection of *B. bacteriovorus* to prey by T4aP, with the tip
195 of the extended pilus clearly in contact with the prey's outer membrane. At the resolution of our
196 cryo-tomograms, no distinctive features were visible at the pilus-prey attachment point (Fig. 2A).
197 Occasionally, we also saw thin fimbriae apparently contacting the outer membrane of the prey cell
198 (Fig. S7).
199
200 Next, we observed predator and prey in close apposition. In some cases, pilus attachments were
201 still visible; in others the pili had retracted completely. In all cases, we observed non-piliated T4aP
202 basal bodies aligned at the contact site, with rose-like complexes nearby (Figs. 2B and S8). In
203 several attachments to *E. coli* minicells, where finer detail could be resolved, we observed that the
204 non-piliated T4aP basal bodies extended through the prey outer membrane, with their extracellular
205 rings apparently embedded in the prey peptidoglycan (PG) (Figs. 2B and S9). At this stage, we
206 began to observe enlargement of the prey periplasm. In agreement with previous studies (Lambert
207 et al., 2011), with rod-shaped prey the contact site was usually located on the side of the prey cell,
208 and on the pole of the predator (Fig. S10A). In some cases, particularly with smaller, spherical *E.*
209 *coli* minicells, the attachment site was displaced slightly off the biting pole onto the side of the
210 predator (Fig. S10B-D).

In the next stage, we observed an electron-dense but relatively unstructured plaque of material (henceforth referred to as the "attachment plaque") at the contact point between the predator and the prey. The diameter of this plaque ranged from 15-70 nm and the thickness usually extended from the predator's OM to the prey's PG cell wall (Figs. 2C, S10C and D), suggesting a modification of the prey cell wall at the predator-prey contact point in agreement with previous reports (Kuru et al., 2017). We often observed nonpiliated T4aP basal bodies near or in the plaque (Fig. S10D), as well as rose-like complexes and, very occasionally, prey-attached pili nearby. While we sometimes observed two or even three *B. bacteriovorus* attached to the same prey cell with T4aP, only one ever formed an attachment plaque, consistent with the committed attachment observed in previous studies (Fig. S11).

At around the same time that the attachment plaque formed at the biting pole, an unexpected process began at the other pole. The sheathed flagellum of the *B. bacteriovorus* was resorbed into the periplasmic space, wrapping around the cell. The process seems to initiate with breakage of the flagellar motor at its OM-embedded ring (the L- (lipopolysaccharide) ring, Fig. S12). The L-ring remained in the OM. Early in the process, the P- (peptidoglycan) ring was still visible around the flagellar rod but was located more than 20 nm from the OM, compared to 10-11 nm in attack-phase cells (Figs. S13 and S14 and Movie S2). Consistent with a decoupling of the P- and L-rings, we observed two examples of *B. bacteriovorus* cells attached to prey with a plaque and with disrupted OM around the flagellum; in both cases, only the P-ring, and not the L-ring, was visible surrounding the rod of the motor (Fig. S15).

As flagellar resorption continued, the motor (lacking the L-ring but including the P-ring and rod) was completely internalized to the periplasm and moved off the cell pole, with the hook and basal portion of the filament entering the periplasm (Figs. 3, S16 and Movie S3). The L-ring still encircled the filament at the junction of OM and flagellar sheath (Figs. 3, S16 and Movie S3). Eventually, most or all of the filament was internalized to the periplasm, wrapping around the cell (Figs. S17, S18 and Movies S4-S7). In some cases, we saw the motor further up the side of the cell. In other cases, we could not find the motor, either because it was degraded or because it was located in a part of the cell not visible due to the effect of the missing wedge of information in cryo-ET (Baumeister, 1999). During the absorption process, the exit point of the flagellum sometimes shifted from the pole up the side of the cell (Figs. S18, S19 and Movie S6). In cells with fully internalized filaments, we could no longer identify L-rings in the outer membrane. In some cases, the wrapped filament broke in the periplasm (Movie S4). Figure S20 summarizes this absorption process based on our cryo-ET data.

Chemosensory arrays remained visible throughout the attachment phase, although they appeared to be partially degraded (smaller in diameter than in attack-phase cells) in some cases. As in attack-phase cells, we observed small, uniformly-sized membrane vesicles in the vicinity of the predator and attached prey (Fig. S21). In some vesicles, densities were visible either inside and/or on the surface (Fig. S21F). We also saw vesicles near the sheath of the flagellum during resorption (Fig. S22).

III- Invasion of the prey periplasm

We captured 18 cryo-tomograms of stalled invasions of *B. bacteriovorus* entering the periplasm of *E. coli* minicells. Note that in these stalled invasions we do not know how long before sample freezing a particular predator entered its prey or whether the non-permissive size of the small prey had incidental effects on the entry process. Still, this paradigm provided an unique opportunity to view fleeting stages of invasion at high resolution. In invasion, the attachment plaque at the contact site was replaced by a portal structure through which the predator entered the prey periplasm (Figs. 4, S23, and Movie S8). This portal ring, which bridged the outer membranes of predator and prey, appeared in cross-section as a thin (<5 nm), dark density extending from the prey's PG layer to the outside of the cell, capping the open end of the prey outer membrane (Figs. 4A and S23A). The height of the portal in cross-section, on the order of a few tens of nanometers, varied between cells, and even on opposite sides of the same cell (e.g. compare Figs. 4A and S23A). In eight examples, we observed what appeared to be prey OM blebbing out from the portal (Movie S9). Consistent with a water-tight seal model, the portal appeared to exert considerable force on the *B. bacteriovorus* cell, as previously observed (Abram et al., 1974), reducing the distance between the outer and inner membranes by ~50% at the entry point compared to elsewhere in the cell, and constricting the deformation-resistant cell wall (Figs. 4B-C, S23B-C). Consistent with previous reports of cell flexibility (Borgnia et al., 2008), we observed that *B. bacteriovorus* could bend considerably to maximally occupy the prey periplasm (Fig. 4A).

In all stalled invasions, we observed that the *B. bacteriovorus* cells had fully degraded their absorbed periplasmic flagella and lacked rose-like complexes and fimbriae. Chemosensory arrays were also partially or completely degraded (Fig. S24). Interestingly, while complexes morphologically similar to non-piliated T4aP basal bodies were still present in the predator, they

lacked the characteristic extracellular ring found at earlier stages of invasion (Fig. S25), and were less abundant than T4aP basal bodies in attack-phase cells. This could be because either the extracellular ring is lost during the invasion process, or these are different complexes, e.g. type II secretion systems.

In two examples where a non-flagellated *B. bacteriovorus* cell was in the vicinity of a lysed prey, we observed knob-like densities on the predator's biting pole (Fig. S26). Given the lysed prey cell nearby and the lack of attack-phase structures such as flagella or chemosensory arrays in the *B. bacteriovorus*, we think it likely that these cells were pulled out of the prey post-invasion during sample preparation. When present, the knob-like structures could be abundant; we identified 23 examples on one cell (Table S2). While leg-like densities could be seen extending from the extracellular domains to the PG layer in individual examples, subtomogram averaging failed to resolve a consistent structure, suggesting flexibility or differing stoichiometry.

Even though entry was incomplete, *B. bacteriovorus* in stalled invasions of *E. coli* minicells showed signs of entering growth phase. Some predators had at least partially decondensed their nucleoids, and the prey cytoplasm was considerably reduced in size, presumably consumed by the predator. Perhaps related to this digestion, we observed multiple vesicles with a consistent size of ~25 nm in the prey periplasm (Figs. 4A and S23A). We cannot tell whether they originated from prey or predator membrane, but their size is identical to those we observed in the vicinity of isolated attack-phase and prey-attached *B. bacteriovorus*.

IV- Growth phase in the bdelloplast

We captured 54 cryo-tomograms of the bdelloplast stage from samples of *B. bacteriovorus* invading *V. cholerae* cells and *E. coli* minicells large enough to accommodate the entire predator. Once the predator fully entered the prey's periplasm, the entry hole was sealed by a scar consisting of an extracellular bubble of what appeared to be membrane and an amorphous electron density associated with the prey OM and PG beneath it (Figs. 5, S27 and S28 and Movies S10-S13). In invaded *V. cholerae*, the prey's (non-functional) flagellum remained attached to the bdelloplast (Figs. 5F and S27B, C). The flagellum remained connected to the part of the motor embedded in the OM and PG: the PL-rings and part of the rod. Presumably these parts were separated from the rest of the motor by periplasmic expansion. We did not observe any motor components still associated with the inner membrane. The fact that flagellar relics remained only on *V. cholerae* bdelloplasts, and not *E. coli*, could be because the flagellar sheath aids in retention. In *V. cholerae* bdelloplasts, we sometimes also observed PL-subcomplexes (without associated filaments) resulting from previous flagellar loss events (Ferreira et al., 2019; Kaplan et al., 2020) (Fig. S27B).

In predators inside bdelloplasts, we saw neither chemosensory arrays nor any relics of flagella, although we occasionally observed filamentous structures in the periplasm that may be remnants of flagellar digestion (Fig. S29). We also sometimes observed these in (flagellated) attack-phase cells (Fig. S3B). Interestingly, they were always located at the pole (the biting pole of attack-phase cells), perhaps reflecting spatial differences in proteolysis. We also could not find any rose-like complexes or T4aP basal bodies with external rings in *B. bacteriovorus* inside bdelloplasts. As in stalled invasions, we did identify putative nonpiliated T4aP basal bodies lacking the external ring. Again, they were less abundant than in attack-phase cells; from 47 cryo-tomograms of stalled invasions or early bdelloplasts, we identified 25 such particles (Table S2). We did occasionally

observe 8-nm-wide cytoplasmic tubes, as seen in other lifecycle stages (Figs. S30). In addition, we saw variously-sized spherical, nested and horseshoe-shaped vesicles in the predator's cytoplasm, morphologically similar to those reported in other species (Dobro et al., 2017) (Fig. S31).

As in stalled invasions of *E. coli* minicells, we observed many uniformly-sized (~25 nm) vesicles in the bdelloplast periplasm (Figs. 5 and S31 and Movies S11-S13). Consistent with active growth, *B. bacteriovorus* nucleoids were less condensed than in earlier stages and, in concert with the prey cytoplasm shrinking, the predator cell elongated and curled to fill most of the bdelloplast (Fig. S32). Contrary to previous observations by traditional EM (Abram et al., 1974), we could not unambiguously identify a connection between the predator OM and prey inner membrane (Figs. S28, S32, S33 and Movies S10-S11).

When nearly all of the prey cytoplasm was consumed, the elongated *B. bacteriovorus* cell divided. The number of progeny depends on the size of the bdelloplast (Fenton et al., 2010a), and we observed two or three progeny cells in *E. coli* and *V. cholerae* prey (e.g., Fig. 5). In a few cases, division produced an extra, small spherical product, in accordance with previous reports (Burnham et al., 1970) (Fig. S34). In some cases, bdelloplasts contained a very dense sphere of material, presumably containing the remnants of the prey cytoplasm (Figs. 5 and S34). In other cases, not even this remained (a characteristic we use to define an "end-stage bdelloplast"). The characteristic ~25 nm vesicles, however, were still present in end-stage bdelloplasts even after no prey cytoplasm remained.

In some elongated or divided *B. bacteriovorus* in end-stage bdelloplasts of *E. coli*, we observed a remarkable hexagonal lattice of ribosomes coating the nucleoid (Fig. 6 and Movies S13-S17). The lattice spacing was ~20 nm, consistent with maximally dense packing of ribosomes (Fig. S35). This arrangement was much more extensive than we and others observed in attack-phase cells (Butan et al., 2011). We measured the distances from ribosomes to the apparent surface of the nucleoid in two tomograms. Of 2,304 ribosomes in one (Fig. 6) and 1,109 in the other (Fig. S36), ~80% were located within 10 nm of the nucleoid surface. By comparison, in a simulation of the same number of randomly-packed 20-nm spheres in the same tomographic volumes (see Materials and Methods), only ~20-25% were expected to be located within 10 nm of the nucleoid surface (Figs. 6E and S36), suggesting that the association we observed does not arise simply by chance. To investigate whether the ordered ribosomes shared the same orientation, we produced an ~4.7 nm-resolution subtomogram average of the ribosomes in a *B. bacteriovorus* cell and mapped it back into the tomographic volume using the positions and orientations determined during averaging. We found that individual particles were apparently randomly oriented on the nucleoid surface (Fig. S37).

Movie S18 offers an animated summary of all stages of the *B. bacteriovorus* predatory lifecycle that we observed in this study.

Discussion

Here we used cryo-ET imaging to reveal the predation cycle of *B. bacteriovorus in situ* at nanometer-scale resolution (Movie S18). Our results contextualize decades of research on BALO predation and uncover many surprising new details of the process.

In addition to previously-characterized structures in attack-phase cells such as the flagellum, poly-phosphate storage granules, highly-condensed nucleoid, chemosensory array, and type IV pili (Borgnia et al., 2008; Butan et al., 2011; Chaban et al., 2018; Evans et al., 2007; Mahmoud and Koval, 2010), we observed several unidentified structures. At all stages of invasion, *B. bacteriovorus* cells contained 8 nm-wide cytoplasmic tubes, typically two per cell. The identity and function of these tubes, which were also seen previously by cryo-ET in attack-phase cells (Borgnia et al., 2008), remains unknown, but they may serve a cytoskeletal role. In a few attack-phase cells, we observed spherical or tubular structures in the periplasm at the biting pole which might be fragments of digested flagella. The biting pole of attack-phase cells also contained abundant fimbriae, shorter (~100 nm or less) and thinner than T4aP and without obvious machinery at their base. Their location suggests a role in prey interaction. Interestingly, mutant strains of *B. bacteriovorus* lacking either T4aP and T4bP genes can still attach to prey (Avidan et al., 2017; Milner et al., 2014); perhaps these fimbriae mediate such adhesion.

The most intriguing new structure we observed is what we call the rose-like complex, present in ~2-3 copies on the biting pole of nearly every attack-phase cell we imaged. The periplasmic portion of the rose-like complex is morphologically similar to a recent structure of a tripartite efflux pump (Alav et al., 2021) and since related *B. bacteriovorus* type I secretion systems (T1SS) secrete

388 enzymes that modify the prey during invasion (Rendulic, 2004), it is possible that the rose-like
389 complex is a T1SS. Consistent with a role in early invasion, we observed rose-like complexes on
390 attack-phase cells and at prey contact sites, but not in cells during or after invasion. The function
391 of the elaborate extracellular domains extending nearly 20 nm out from the cell is of particular
392 interest; perhaps they interact with, or breach, the prey envelope.
393
394 Another machine with a notable extracellular domain is the T4aP basal body. The pili observed on
395 the biting pole of *B. bacteriovorus* in early micrographs (Abram and Davis, 1970; Abram et al.,
396 1974; Shilo, 1969) were previously identified as T4aP by mutant analysis and immunolocalization
397 (Evans et al., 2007; Mahmoud and Koval, 2010). Our higher-resolution imaging here revealed a
398 novel extracellular ring surrounding the base of the pilus, not seen in previous subtomogram
399 averages of related T4aP in *Thermus thermophilus* and *Myxococcus xanthus* (Chang et al., 2016;
400 Gold et al., 2015). The ring was also present in non-piliated basal bodies, indicating that it is stable
401 in the absence of the pilus. Interestingly, these extracellular densities were observed on attack-
402 phase cells in a previous cryo-ET study, but their relation to T4aP was not resolved (Borgnia et al.,
403 2008). We observed some non-piliated complexes lacking the extracellular ring, both in attack-
404 phase cells and in bdelloplasts, where no complexes with the outer ring were observed. It is
405 possible that these complexes are not T4aP, but rather a related machine containing a Secretin pore
406 in the outer membrane, such as a type II secretion system, which is structurally similar (Ghosal et
407 al., 2019b) and thought to be involved in *B. bacteriovorus* secretion (Dori-Bachash et al., 2008;
408 Rendulic, 2004). In addition, *B. bacteriovorus* also contains a large repertoire of T4bP genes,
409 which are dispensable for attachment but required for invasion (Avidan et al., 2017; Schwudke et
410 al., 2005). Their products have not been located on the cell and it is possible that some or all of the

411 ring-less basal bodies we saw were T4bP. Alternatively, the extracellular ring may be a transient
412 component of the *B. bacteriovorus* T4aP, perhaps dissociating during the prey entry process.
413
414 The pilin protein PilA is required for invasion and T4aP have been suggested to pull cells into prey,
415 perhaps by attaching to the cell wall (Evans et al., 2007; Mahmoud and Koval, 2010; Milner et al.,
416 2014), but mutants lacking the disassembly PilT ATPase are still capable of invasion (Chanyi and
417 Koval, 2014) and the role of T4aP in the process remains a major open question in the field
418 (Sockett, 2009). In our tomograms, multiple T4aP can be seen attached to prey cells and clearly
419 exerting force as they retracted, pulling the prey OM and PG into close contact with the predator.
420 As the membranes were brought into contact, the shortening pili fully disassembled, leaving empty
421 basal bodies. Interestingly, these non-piliated basal bodies continued to mediate attachment and
422 could be seen extending through the prey OM, with their extracellular rings located in the PG layer
423 of the prey, suggesting the function of this novel component. Our results thus suggest that pili
424 themselves do not drive entry, but rather force the initial connection. If the basal bodies without
425 external rings we observed in bdelloplasts were in fact T4aP, it is possible that the rings remained
426 embedded in the prey PG.
427
428 With a few exceptions noted by (Lambert et al., 2006), *B. bacteriovorus* are known to lose their
429 flagella when entering prey. Our images reveal a surprising mechanism: while attached to a prey
430 cell, the flagellar motor is broken at the L-ring and the filament absorbed into the predator's
431 periplasm, where it is digested. This mechanism differs from all previous observations of flagellar
432 loss due to lifecycle-programmed ejection, response to nutrient deprivation or mechanical
433 breakage, all of which leave a stable subcomplex of the P- and L-rings in the cell wall and outer

membrane (Ferreira et al., 2019; Kaplan et al., 2019, 2020, 2021b, 2021b; Zhu and Gao, 2020; Zhu et al., 2019; Zhuang and Lo, 2020; Zhuang et al., 2020). It will be interesting to see whether the *B. bacteriovorus* motor lacks the inter-subunit interactions that likely stabilize the PL-subcomplex in other species (Johnson et al., 2021; Tan et al., 2021; Yamaguchi et al., 2020). This process also differs from the breakage of the prey flagellum that occurs as the periplasmic space is expanded into the bdelloplast. In that case, we see that the flagellum remains anchored to the cell by a stub of the motor embedded in the outer membrane. Why the hook/filament is not lost is unclear; perhaps it is locked into the remodeled PG. This process is reminiscent of that recently observed in other species upon cell lysis, where the cytoplasmic flagellar switch complex is lost, while the periplasmic and extracellular components remain (Kaplan et al., 2021c).

How does *B. bacteriovorus* absorb its flagellum into the periplasm? It is unlikely to be pulled from the motor, which we occasionally saw drift partway up the side of the cell before being fully degraded. Our observation of filaments partially absorbed up to a junction on the side of the cell suggests that the process involves zippering of the flagellar sheath and the outer membrane. Perhaps this is related to the unique lipid composition of the sheath, which is predicted to be even more fluid than the rest of the outer membrane (Thomashow and Rittenberg, 1985b). The vesicles we observed in the vicinity of some absorbed flagella are consistent with previous reports that rotation of sheathed flagella can lead to shedding of outer membrane vesicles (Aschtgen et al., 2016; Brennan et al., 2014). However, we do not know whether the vesicles formed because the motor was still rotating during absorption or due to the absorption process itself.

Other bacterial species have been observed to wrap their extracellular (unsheathed) flagella around themselves (Alirezaeizanjani et al., 2020; Cohen et al., 2020; Constantino et al., 2018; Hintsche et al., 2017; Kühn et al., 2017; Tian et al., 2022). This behavior, which *Shewanella putrefaciens* uses to burrow back out of a tight spot when stuck, is triggered by a mechanical instability in the flagellum that buckles it when the cell can no longer move to alleviate the torque of flagellar rotation (Kühn et al., 2017). Such a situation likely occurs when a *B. bacteriovorus* cell attaches to a prey. Brief continuing flagellar rotation could conceivably wrap the filament around the cell, where fusion of the outer membrane and sheath would bring it into the periplasm. Such increased resistance is consistent with the lateral shift of the biting pole we sometimes observed on attached *B. bacteriovorus* cells. Interestingly, it was recently shown that a discontinuous flagellar filament formed by two different flagellins facilitates screw-like motility in *S. putrefaciens* (Kühn et al., 2018), and is key to wrapping in *Campylobacter jejuni* (Cohen et al., 2020). Multiple flagellins similarly make up distinct segments of the *B. bacteriovorus* flagellum (Thomashow and Rittenberg, 1985a); the reason for this was unknown but now we speculate that it may facilitate flagellar recycling.

A major open question is the nature of the pore through which *B. bacteriovorus* enter their prey. Secreted PG-remodeling enzymes, presumably part of the dense plaque we observe at the attachment site that extends to the prey cell wall, are known to create, and subsequently seal, a reinforced circular porthole in the prey PG (see figures 2 and 3 in (Kuru et al., 2017)). How the prey outer membrane is modified remains more of a mystery. Prey cells remain intact and transcriptionally active throughout the initial entry process (Lambert et al., 2010a), so it was proposed that the membranes of prey and predator must fuse (Negus et al., 2017). Instead, we

479 observed what seems to be a proteinaceous collar curving out from the prey PG to seal the hole in
480 the outer membrane and prevent interaction of the two membranes. Presumably this structure is
481 associated with the PG remodeling enzymes, and may even be a modified and reinforced extension
482 of the cell wall, as suggested by (Abram et al., 1974). The portal is dynamic, expanding and
483 contracting to match the cross-section of the cell passing through it, and its height varied between
484 cells (and even on opposite sides of the same cell). As was also seen by traditional thin-section
485 TEM (Abram et al., 1974), the portal exerted considerable force on the *B. bacteriovorus* cell,
486 deforming its PG layer, consistent with a water-tight seal between the cells.
487
488 What provides the force for entry remains enigmatic. Over several decades, various models have
489 been proposed, including flagellar rotation (Stolp and Starr, 1963), retraction of T4aP attached to
490 the prey cell wall (Evans et al., 2007; Mahmoud and Koval, 2010), and attachment to the prey
491 inner membrane as osmotic pressure rapidly expands the periplasm (Abram et al., 1974). Our
492 results rule out all of these models. We see that the *B. bacteriovorus* flagellum is broken, and at
493 least partially absorbed, prior to entry. Similarly, pili are fully disassembled prior to entry. And
494 finally, we see prey periplasmic expansion even before entry, presumably due to secreted enzymes
495 that de-crosslink and sculpt the prey PG during entry (Lerner et al., 2012), with no visible
496 connection between the predator and the now-distant prey inner membrane. It is possible that an
497 expanding periplasmic space provides a suction force. It is also possible that an active mechanism
498 walks the connection point with the portal down the *B. bacteriovorus* cell.
499
500 Following predator entry, we saw that the portal is sealed by a scar of electron dense material,
501 likely related to the resealing of the PG sacculus (Kuru et al., 2017; Snellen and Starr, 1974), with

a protruding bubble of what appears to be membrane. While previous, traditional EM imaging also observed an electron-dense ring at the sealed penetration pore (Shilo, 1969), no associated bubble was observed, perhaps reflecting the improved preservation and hydration of membrane structures by cryo-EM. Given the blebs around the invasion portal we noticed on some prey cells in stalled invasions, it may be prey OM. Alternatively, it may be outer membrane pinched off from the end of the invading predator. *B. bacteriovorus* has a highly labile OM, as we saw both with absorption of the sheathed flagellum and in occasional highly-curved cells where the outer membrane fused into a sac, and consistent with previous lipid analysis of its unique membrane (Lambert et al., 2008). In either case, the bubble must be somehow tethered to the seal, perhaps through membrane-embedded protein complexes.

While we did not see the connections to the prey cytoplasm during entry observed by (Abram et al., 1974), we did see a few examples of the predator outer and prey inner membranes in close proximity in the bdelloplast. In most cases, however, we only observed vesicles in the bdelloplast periplasm, suggesting that this may be a mechanism for nutrient transfer. Compared to membrane vesicles of other species (Kaplan et al., 2021d; Toyofuku et al., 2019), these vesicles were notable for their relatively small and uniform size (~25 nm in diameter). Similar small periplasmic vesicles may be present in previous traditional EM images, but interpretation is limited by the membrane disruption of that sample preparation (Abram et al., 1974). In our tomograms, we cannot tell which cell(s) are producing the vesicles in bdelloplasts, but we also observed them near isolated attack-phase cells as well as budding from *B. bacteriovorus* attached to prey. We also observed them in end-stage bdelloplasts where no remaining prey inner membrane was visible. *B. bacteriovorus* is known to translocate a pore protein from its outer membrane to the prey inner membrane (Tudor

525 and Karp, 1994); perhaps similar transferred machinery produces vesicles to deliver prey
526 cytoplasmic content, and lipids, to the growing predator.
527
528 Following complete consumption of the prey, we observed a striking hexagonal lattice of
529 ribosomes on the surface of the *B. bacteriovorus* condensed nucleoid(s). Similar, though more
530 limited, ribosome associations were previously observed in attack phase, particularly in a *B.*
531 *bacteriovorus* mutant with an even more tightly condensed nucleoid than wild-type cells (Borgnia
532 et al., 2008; Butan et al., 2011), and in some attack-phase cells in this study. One possibility for
533 this ribosome lattice is that it is a depletion effect resulting from entropic forces encouraging large
534 objects to aggregate on a surface (Asakura and Oosawa, 1954, 1958; Rocha et al., 2020). However,
535 we did not observe the effect on other cell surfaces such as the inner membrane, nor in other stages
536 of the cell cycle, so we think this unlikely. Eukaryotic ribosomes have been observed to crystallize
537 in hypothermic conditions (Byers, 1967), but we see no relationship between the orientation of
538 neighboring particles consistent with a crystal, or with a polysome (Brandt et al., 2009). We think
539 a more likely possibility is that the ribosomes are independently translating transcripts from the
540 condensing nucleoid. The switch from growth phase to attack phase involves a transcriptional shift
541 activating a few hundred genes, and inactivating many more (Karunker et al., 2013; Lambert et al.,
542 2010b). The highly condensed attack-phase nucleoid excludes even small monomeric proteins
543 (Kaljević et al., 2021), so the ribosomes we observe on the surface may be, or recently have been,
544 coupled to transcribing polymerases.
545
546 Together, our results provide the most complete view to date of the unique structures that enable
547 the complex lifecycle of this endobiotic bacterial predator, and raise new questions. We hope our

548 work spurs further study of this fascinating process and informs potential future applications of
549 bacterial predators as living antibiotics (Atterbury and Tyson, 2021).

References

Abram, D., and Davis, B.K. (1970). Structural Properties and Features of Parasitic *Bdellovibrio bacteriovorus*. J Bacteriol *104*, 948–965. https://doi.org/10.1128/jb.104.2.948-965.1970.

Abram, D., e Melo, J.C., and Chou, D. (1974). Penetration of *Bdellovibrio bacteriovorus* into Host Cells. J Bacteriol *118*, 663–680. https://doi.org/10.1128/jb.118.2.663-680.1974.

Alav, I., Kobylka, J., Kuth, M.S., Pos, K.M., Picard, M., Blair, J.M.A., and Bavro, V.N. (2021). Structure, Assembly, and Function of Tripartite Efflux and Type 1 Secretion Systems in Gram-Negative Bacteria. Chem. Rev. *121*, 5479–5596. https://doi.org/10.1021/acs.chemrev.1c00055.

Alirezaeizanjani, Z., Großmann, R., Pfeifer, V., Hintsche, M., and Beta, C. (2020). Chemotaxis strategies of bacteria with multiple run modes. Sci. Adv. *6*, eaaz6153. https://doi.org/10.1126/sciadv.aaz6153.

Asakura, S., and Oosawa, F. (1954). On Interaction between Two Bodies Immersed in a Solution of Macromolecules. The Journal of Chemical Physics *22*, 1255–1256. https://doi.org/10.1063/1.1740347.

Asakura, S., and Oosawa, F. (1958). Interaction between particles suspended in solutions of macromolecules. J. Polym. Sci. *33*, 183–192. https://doi.org/10.1002/pol.1958.1203312618.

Aschtgen, M.-S., Lynch, J.B., Koch, E., Schwartzman, J., McFall-Ngai, M., and Ruby, E. (2016). Rotation of Vibrio fischeri Flagella Produces Outer Membrane Vesicles That Induce Host Development. Journal of Bacteriology *198*, 2156–2165. https://doi.org/10.1128/JB.00101-16.

Atterbury, R.J., and Tyson, J. (2021). Predatory bacteria as living antibiotics – where are we now? Microbiology *167*. https://doi.org/10.1099/mic.0.001025.

Avidan, O., Petrenko, M., Becker, R., Beck, S., Linscheid, M., Pietrokovski, S., and Jurkevitch, E. (2017). Identification and Characterization of Differentially-Regulated Type IVb Pilin Genes Necessary for Predation in Obligate Bacterial Predators. Sci Rep *7*, 1013. https://doi.org/10.1038/s41598-017-00951-w.

Banks, E.J., Valdivia-Delgado, M., Biboy, J., Wilson, A., Cadby, I.T., Vollmer, W., Lambert, C., Lovering, A.L., and Sockett, R.E. (2022). Asymmetric peptidoglycan editing generates cell curvature in Bdellovibrio predatory bacteria. Nat Commun *13*, 1509. https://doi.org/10.1038/s41467-022-29007-y.

Baumeister, W. (1999). Electron tomography of molecules and cells. Trends in Cell Biology *9*, 81–85. https://doi.org/10.1016/S0962-8924(98)01423-8.

Bonfiglio, G., Neroni, B., Radocchia, G., Marazzato, M., Pantanella, F., and Schippa, S. (2020). Insight into the Possible Use of the Predator Bdellovibrio bacteriovorus as a Probiotic. Nutrients *12*, 2252. https://doi.org/10.3390/nu12082252.

584 Borgnia, M.J., Subramaniam, S., and Milne, J.L.S. (2008). Three-Dimensional Imaging of the
585 Highly Bent Architecture of Bdellovibrio bacteriovorus by Using Cryo-Electron Tomography.
586 JB *190*, 2588–2596. https://doi.org/10.1128/JB.01538-07.

587 Brandt, F., Etchells, S.A., Ortiz, J.O., Elcock, A.H., Hartl, F.U., and Baumeister, W. (2009). The
588 Native 3D Organization of Bacterial Polysomes. Cell *136*, 261–271.
589 https://doi.org/10.1016/j.cell.2008.11.016.

590 Bratanis, E., Andersson, T., Lood, R., and Bukowska-Faniband, E. (2020). Biotechnological
591 Potential of Bdellovibrio and Like Organisms and Their Secreted Enzymes. Front. Microbiol. *11*,
592 662. https://doi.org/10.3389/fmicb.2020.00662.

593 Brennan, C.A., Hunt, J.R., Kremer, N., Krasity, B.C., Apicella, M.A., McFall-Ngai, M.J., and
594 Ruby, E.G. (2014). A model symbiosis reveals a role for sheathed-flagellum rotation in the
595 release of immunogenic lipopolysaccharide. ELife *3*. https://doi.org/10.7554/eLife.01579.

596 Bukowska-Faniband, E., Andersson, T., and Lood, R. (2020). Studies on Bd0934 and Bd3507,
597 Two Secreted Nucleases from *Bdellovibrio bacteriovorus* , Reveal Sequential Release of
598 Nucleases during the Predatory Cycle. J Bacteriol *202*, e00150-20, /jb/202/18/JB.00150-20.atom.
599 https://doi.org/10.1128/JB.00150-20.

600 Burnham, J.C., Hashimoto, T., and Conti, S.F. (1968). Electron microscopic observations on the
601 penetration of Bdellovibrio bacteriovorus into gram-negative bacterial hosts. J Bacteriol *96*,
602 1366–1381. https://doi.org/10.1128/JB.96.4.1366-1381.1968.

603 Burnham, J.C., Hashimoto, T., and Conti, S.F. (1970). Ultrastructure and Cell Division of a
604 Facultatively Parasitic Strain of *Bdellovibrio bacteriovorus*. J Bacteriol *101*, 997–1004.
605 https://doi.org/10.1128/jb.101.3.997-1004.1970.

606 Butan, C., Hartnell, L.M., Fenton, A.K., Bliss, D., Sockett, R.E., Subramaniam, S., and Milne,
607 J.L.S. (2011). Spiral Architecture of the Nucleoid in Bdellovibrio bacteriovorus. Journal of
608 Bacteriology *193*, 1341–1350. https://doi.org/10.1128/JB.01061-10.

609 Byers, B. (1967). Structure and formation of ribosome crystals in hypothermic chick embryo
610 cells. Journal of Molecular Biology *26*, 155–167. https://doi.org/10.1016/0022-2836(67)90288-4.

611 Calakli, F., and Taubin, G. (2012). SSD-C: Smooth Signed Distance Colored Surface
612 Reconstruction. In Expanding the Frontiers of Visual Analytics and Visualization, J. Dill, R.
613 Earnshaw, D. Kasik, J. Vince, and P.C. Wong, eds. (London: Springer London), pp. 323–338.

614 Capeness, M.J., Lambert, C., Lovering, A.L., Till, R., Uchida, K., Chaudhuri, R., Alderwick,
615 L.J., Lee, D.J., Swarbreck, D., Liddell, S., et al. (2013). Activity of Bdellovibrio Hit Locus
616 Proteins, Bd0108 and Bd0109, Links Type IVa Pilus Extrusion/Retraction Status to Prey-
617 Independent Growth Signalling. PLoS ONE *8*, e79759.
618 https://doi.org/10.1371/journal.pone.0079759.

619 Caulton, S.G., and Lovering, A.L. (2020). Bacterial invasion and killing by predatory
620 Bdellovibrio primed by predator prey cell recognition and self protection. Current Opinion in
621 Microbiology *56*, 74–80. https://doi.org/10.1016/j.mib.2020.07.002.

622 Cavallo, F.M., Jordana, L., Friedrich, A.W., Glasner, C., and van Dijl, J.M. (2021). *Bdellovibrio*
623 *bacteriovorus* : a potential 'living antibiotic' to control bacterial pathogens. Critical Reviews in
624 Microbiology 1–17. https://doi.org/10.1080/1040841X.2021.1908956.

625 Chaban, B., Coleman, I., and Beeby, M. (2018). Evolution of higher torque in Campylobacter-
626 type bacterial flagellar motors. Scientific Reports *8*. https://doi.org/10.1038/s41598-017-18115-
627 1.

628 Chang, Y.-W., Rettberg, L.A., Treuner-Lange, A., Iwasa, J., Søgaard-Andersen, L., and Jensen,
629 G.J. (2016). Architecture of the type IVa pilus machine. Science *351*, aad2001.
630 https://doi.org/10.1126/science.aad2001.

631 Chang, Y.-W., Kjær, A., Ortega, D.R., Kovacikova, G., Sutherland, J.A., Rettberg, L.A., Taylor,
632 R.K., and Jensen, G.J. (2017). Architecture of the Vibrio cholerae toxin-coregulated pilus
633 machine revealed by electron cryotomography. Nature Microbiology *2*.
634 https://doi.org/10.1038/nmicrobiol.2016.269.

635 Chanyi, R.M., and Koval, S.F. (2014). Role of Type IV Pili in Predation by Bdellovibrio
636 bacteriovorus. PLoS ONE *9*, e113404. https://doi.org/10.1371/journal.pone.0113404.

637 Chen, M., Bell, J.M., Shi, X., Sun, S.Y., Wang, Z., and Ludtke, S.J. (2019). A complete data
638 processing workflow for cryo-ET and subtomogram averaging. Nat Methods *16*, 1161–1168.
639 https://doi.org/10.1038/s41592-019-0591-8.

640 Chreifi, G., Chen, S., Metskas, L.A., Kaplan, M., and Jensen, G.J. (2019). Rapid tilt-series
641 acquisition for electron cryotomography. Journal of Structural Biology *205*, 163–169.
642 https://doi.org/10.1016/j.jsb.2018.12.008.

643 Cohen, E.J., Nakane, D., Kabata, Y., Hendrixson, D.R., Nishizaka, T., and Beeby, M. (2020).
644 Campylobacter jejuni motility integrates specialized cell shape, flagellar filament, and motor, to
645 coordinate action of its opposed flagella. PLoS Pathog *16*, e1008620.
646 https://doi.org/10.1371/journal.ppat.1008620.

647 Constantino, M.A., Jabbarzadeh, M., Fu, H.C., Shen, Z., Fox, J.G., Haesebrouck, F., Linden,
648 S.K., and Bansil, R. (2018). Bipolar lophotrichous Helicobacter suis combine extended and
649 wrapped flagella bundles to exhibit multiple modes of motility. Sci Rep *8*, 14415.
650 https://doi.org/10.1038/s41598-018-32686-7.

651 Davidov, Y., and Jurkevitch, E. (2009). Predation between prokaryotes and the origin of
652 eukaryotes. BioEssays *31*, 748–757. https://doi.org/10.1002/bies.200900018.

653 Ding, H.J., Oikonomou, C.M., and Jensen, G.J. (2015). The Caltech Tomography Database and
654 Automatic Processing Pipeline. Journal of Structural Biology *192*, 279–286.
655 https://doi.org/10.1016/j.jsb.2015.06.016.

656 Dobro, M.J., Oikonomou, C.M., Piper, A., Cohen, J., Guo, K., Jensen, T., Tadayon, J.,
657 Donermeyer, J., Park, Y., Solis, B.A., et al. (2017). Uncharacterized Bacterial Structures
658 Revealed by Electron Cryotomography. Journal of Bacteriology *199*.
659 https://doi.org/10.1128/JB.00100-17.

660 Dori-Bachash, M., Dassa, B., Pietrokovski, S., and Jurkevitch, E. (2008). Proteome-Based
661 Comparative Analyses of Growth Stages Reveal New Cell Cycle-Dependent Functions in the
662 Predatory Bacterium *Bdellovibrio bacteriovorus*. Appl Environ Microbiol *74*, 7152–7162.
663 https://doi.org/10.1128/AEM.01736-08.

664 Eisenstein, F., Danev, R., and Pilhofer, M. (2019). Improved applicability and robustness of fast
665 cryo-electron tomography data acquisition. Journal of Structural Biology *208*, 107–114.
666 https://doi.org/10.1016/j.jsb.2019.08.006.

667 Erken, M., Lutz, C., and McDougald, D. (2013). The Rise of Pathogens: Predation as a Factor
668 Driving the Evolution of Human Pathogens in the Environment. Microb Ecol *65*, 860–868.
669 https://doi.org/10.1007/s00248-013-0189-0.

670 Evans, K.J., Lambert, C., and Sockett, R.E. (2007). Predation by Bdellovibrio bacteriovorus
671 HD100 Requires Type IV Pili. JB *189*, 4850–4859. https://doi.org/10.1128/JB.01942-06.

672 Fenton, A.K., Kanna, M., Woods, R.D., Aizawa, S.-I., and Sockett, R.E. (2010a). Shadowing the
673 Actions of a Predator: Backlit Fluorescent Microscopy Reveals Synchronous Nonbinary
674 Septation of Predatory Bdellovibrio inside Prey and Exit through Discrete Bdelloplast Pores. JB
675 *192*, 6329–6335. https://doi.org/10.1128/JB.00914-10.

676 Fenton, A.K., Hobley, L., Butan, C., Subramaniam, S., and Sockett, R.E. (2010b). A coiled-coil-
677 repeat protein 'Ccrp' in Bdellovibrio bacteriovorus prevents cellular indentation, but is not
678 essential for vibroid cell morphology: CCRP protein in Bdellovibrio. FEMS Microbiology
679 Letters *313*, 89–95. https://doi.org/10.1111/j.1574-6968.2010.02125.x.

680 Ferreira, J.L., Gao, F.Z., Rossmann, F.M., Nans, A., Brenzinger, S., Hosseini, R., Wilson, A.,
681 Briegel, A., Thormann, K.M., Rosenthal, P.B., et al. (2019). γ-proteobacteria eject their polar
682 flagella under nutrient depletion, retaining flagellar motor relic structures. PLOS Biology *17*,
683 e3000165. https://doi.org/10.1371/journal.pbio.3000165.

684 Friedrich, C., Bulyha, I., and Søgaard-Andersen, L. (2014). Outside-In Assembly Pathway of the
685 Type IV Pilus System in Myxococcus xanthus. J Bacteriol *196*, 378–390.
686 https://doi.org/10.1128/JB.01094-13.

687 Ghosal, D., Kaplan, M., Chang, Y.-W., and Jensen, G.J. (2019a). In Situ Imaging and Structure
688 Determination of Bacterial Toxin Delivery Systems Using Electron Cryotomography. In
689 Legionella, C. Buchrieser, and H. Hilbi, eds. (New York, NY: Springer New York), pp. 249–
690 265.

691 Ghosal, D., Kim, K.W., Zheng, H., Kaplan, M., Truchan, H.K., Lopez, A.E., McIntire, I.E.,
692 Vogel, J.P., Cianciotto, N.P., and Jensen, G.J. (2019b). In vivo structure of the Legionella type II

693 secretion system by electron cryotomography. Nature Microbiology
694 https://doi.org/10.1038/s41564-019-0603-6.

695 Gold, V.A., Salzer, R., Averhoff, B., and Kühlbrandt, W. (2015). Structure of a type IV pilus
696 machinery in the open and closed state. ELife *4*. https://doi.org/10.7554/eLife.07380.

697 Hagen, W.J.H., Wan, W., and Briggs, J.A.G. (2017). Implementation of a cryo-electron
698 tomography tilt-scheme optimized for high resolution subtomogram averaging. J. Struct. Biol.
699 *197*, 191–198. https://doi.org/10.1016/j.jsb.2016.06.007.

700 Harding, C.J., Huwiler, S.G., Somers, H., Lambert, C., Ray, L.J., Till, R., Taylor, G., Moynihan,
701 P.J., Sockett, R.E., and Lovering, A.L. (2020). A lysozyme with altered substrate specificity
702 facilitates prey cell exit by the periplasmic predator Bdellovibrio bacteriovorus. Nat Commun *11*,
703 4817. https://doi.org/10.1038/s41467-020-18139-8.

704 Harini, K., Ajila, V., and Hegde, S. (2013). Bdellovibrio bacteriovorus : A future antimicrobial
705 agent? J Indian Soc Periodontol *17*, 823. https://doi.org/10.4103/0972-124X.124534.

706 Heumann, J.M., Hoenger, A., and Mastronarde, D.N. (2011). Clustering and variance maps for
707 cryo-electron tomography using wedge-masked differences. Journal of Structural Biology *175*,
708 288–299. https://doi.org/10.1016/j.jsb.2011.05.011.

709 Hintsche, M., Waljor, V., Großmann, R., Kühn, M.J., Thormann, K.M., Peruani, F., and Beta, C.
710 (2017). A polar bundle of flagella can drive bacterial swimming by pushing, pulling, or coiling
711 around the cell body. Sci Rep *7*, 16771. https://doi.org/10.1038/s41598-017-16428-9.

712 Hobley, L., Fung, R.K.Y., Lambert, C., Harris, M.A.T.S., Dabhi, J.M., King, S.S., Basford, S.M.,
713 Uchida, K., Till, R., Ahmad, R., et al. (2012). Discrete Cyclic di-GMP-Dependent Control of
714 Bacterial Predation versus Axenic Growth in Bdellovibrio bacteriovorus. PLoS Pathog *8*,
715 e1002493. https://doi.org/10.1371/journal.ppat.1002493.

716 Iebba, V., Totino, V., Santangelo, F., Gagliardi, A., Ciotoli, L., Virga, A., Ambrosi, C., Pompili,
717 M., De Biase, R.V., Selan, L., et al. (2014). Bdellovibrio bacteriovorus directly attacks
718 Pseudomonas aeruginosa and Staphylococcus aureus Cystic fibrosis isolates. Front. Microbiol. *5*.
719 https://doi.org/10.3389/fmicb.2014.00280.

720 Iida, Y., Hobley, L., Lambert, C., Fenton, A.K., Sockett, R.E., and Aizawa, S.-I. (2009). Roles of
721 Multiple Flagellins in Flagellar Formation and Flagellar Growth Post Bdelloplast Lysis in
722 Bdellovibrio bacteriovorus. Journal of Molecular Biology *394*, 1011–1021.
723 https://doi.org/10.1016/j.jmb.2009.10.003.

724 Jewett, A. (2021a). Jewett, AI, VISFD Software, https://doi.org/10.5281/zenodo.5559243.

725 Jewett, A. (2021b). Jewett, AI., VISFD Tutorials, https://doi.org/10.5281/zenodo.5758648.

726 Johnson, S., Furlong, E.J., Deme, J.C., Nord, A.L., Caesar, J.J.E., Chevance, F.F.V., Berry,
727 R.M., Hughes, K.T., and Lea, S.M. (2021). Molecular structure of the intact bacterial flagellar
728 basal body. Nat Microbiol *6*, 712–721. https://doi.org/10.1038/s41564-021-00895-y.

729 Kaljević, J., Saaki, T.N.V., Govers, S.K., Remy, O., van Raaphorst, R., Lamot, T., and Laloux,
730 G. (2021). Chromosome choreography during the non-binary cell cycle of a predatory bacterium.
731 Current Biology *31*, 3707-3720.e5. https://doi.org/10.1016/j.cub.2021.06.024.

732 Kaplan, M., Subramanian, P., Ghosal, D., Oikonomou, C.M., Pirbadian, S., Starwalt-Lee, R.,
733 Mageswaran, S.K., Ortega, D.R., Gralnick, J.A., El-Naggar, M.Y., et al. (2019). *In situ* imaging
734 of the bacterial flagellar motor disassembly and assembly processes. The EMBO Journal
735 e100957. https://doi.org/10.15252/embj.2018100957.

736 Kaplan, M., Sweredoski, M.J., Rodrigues, J.P.G.L.M., Tocheva, E.I., Chang, Y.-W., Ortega,
737 D.R., Beeby, M., and Jensen, G.J. (2020). Bacterial flagellar motor PL-ring disassembly
738 subcomplexes are widespread and ancient. Proceedings of the National Academy of Sciences
739 201916935. https://doi.org/10.1073/pnas.1916935117.

740 Kaplan, M., Nicolas, W.J., Zhao, W., Carter, S.D., Metskas, L.A., Chreifi, G., Ghosal, D., and
741 Jensen, G.J. (2021a). In Situ Imaging and Structure Determination of Biomolecular Complexes
742 Using Electron Cryo-Tomography. In CryoEM, T. Gonen, and B.L. Nannenga, eds. (New York,
743 NY: Springer US), pp. 83–111.

744 Kaplan, M., Wang, Y., Chreifi, G., Zhang, L., Chang, Y.-W., and Jensen, G.J. (2021b).
745 Programmed flagellar ejection in Caulobacter crescentus leaves PL-subcomplexes. Journal of
746 Molecular Biology 167004. https://doi.org/10.1016/j.jmb.2021.167004.

747 Kaplan, M., Tocheva, E.I., Briegel, A., Dobro, M.J., Chang, Y.-W., Subramanian, P., McDowall,
748 A.W., Beeby, M., and Jensen, G.J. (2021c). Loss of the Bacterial Flagellar Motor Switch
749 Complex upon Cell Lysis. MBio e0029821. https://doi.org/10.1128/mBio.00298-21.

750 Kaplan, M., Chreifi, G., Metskas, L.A., Liedtke, J., Wood, C.R., Oikonomou, C.M., Nicolas,
751 W.J., Subramanian, P., Zacharoff, L.A., Wang, Y., et al. (2021d). In situ imaging of bacterial
752 outer membrane projections and associated protein complexes using electron cryo-tomography.
753 ELife *10*, e73099. https://doi.org/10.7554/eLife.73099.

754 Karunker, I., Rotem, O., Dori-Bachash, M., Jurkevitch, E., and Sorek, R. (2013). A Global
755 Transcriptional Switch between the Attack and Growth Forms of Bdellovibrio bacteriovorus.
756 PLoS ONE *8*, e61850. https://doi.org/10.1371/journal.pone.0061850.

757 Kazhdan, M., and Hoppe, H. (2013). Screened poisson surface reconstruction. ACM Trans.
758 Graph. *32*, 1–13. https://doi.org/10.1145/2487228.2487237.

759 Kremer, J.R., Mastronarde, D.N., and McIntosh, J.R. (1996). Computer visualization of three-
760 dimensional image data using IMOD. J. Struct. Biol. *116*, 71–76.
761 https://doi.org/10.1006/jsbi.1996.0013.

762 Kühn, M.J., Schmidt, F.K., Eckhardt, B., and Thormann, K.M. (2017). Bacteria exploit a
763 polymorphic instability of the flagellar filament to escape from traps. Proceedings of the
764 National Academy of Sciences *114*, 6340–6345. https://doi.org/10.1073/pnas.1701644114.

765 Kühn, M.J., Schmidt, F.K., Farthing, N.E., Rossmann, F.M., Helm, B., Wilson, L.G., Eckhardt,
766 B., and Thormann, K.M. (2018). Spatial arrangement of several flagellins within bacterial
767 flagella improves motility in different environments. Nat Commun *9*, 5369.
768 https://doi.org/10.1038/s41467-018-07802-w.

769 Kuru, E., Lambert, C., Rittichier, J., Till, R., Ducret, A., Derouaux, A., Gray, J., Biboy, J.,
770 Vollmer, W., VanNieuwenhze, M., et al. (2017). Fluorescent D-amino-acids reveal bi-cellular
771 cell wall modifications important for Bdellovibrio bacteriovorus predation. Nat Microbiol *2*,
772 1648–1657. https://doi.org/10.1038/s41564-017-0029-y.

773 Laloux, G. (2020). Shedding Light on the Cell Biology of the Predatory Bacterium Bdellovibrio
774 bacteriovorus. Front. Microbiol. *10*, 3136. https://doi.org/10.3389/fmicb.2019.03136.

775 Lambert, C., and Sockett, R.E. (2008). Laboratory Maintenance of *Bdellovibrio*. Current
776 Protocols in Microbiology *9*, 7B.2.1-7B.2.13.
777 https://doi.org/10.1002/9780471729259.mc07b02s9.

778 Lambert, C., Evans, K.J., Till, R., Hobley, L., Capeness, M., Rendulic, S., Schuster, S.C.,
779 Aizawa, S.-I., and Sockett, R.E. (2006). Characterizing the flagellar filament and the role of
780 motility in bacterial prey-penetration by Bdellovibrio bacteriovorus. Mol Microbiol *60*, 274–286.
781 https://doi.org/10.1111/j.1365-2958.2006.05081.x.

782 Lambert, C., Hobley, L., Chang, C.-Y., Fenton, A., Capeness, M., and Sockett, L. (2008). A
783 Predatory Patchwork: Membrane and Surface Structures of Bdellovibrio bacteriovorus. In
784 Advances in Microbial Physiology, (Elsevier), pp. 313–361.

785 Lambert, C., Ivanov, P., and Sockett, R.E. (2010a). A Transcriptional "Scream" Early Response
786 of E. coli Prey to Predatory Invasion by Bdellovibrio. Curr Microbiol *60*, 419–427.
787 https://doi.org/10.1007/s00284-009-9559-8.

788 Lambert, C., Chang, C.-Y., Capeness, M.J., and Sockett, R.E. (2010b). The First Bite— Profiling
789 the Predatosome in the Bacterial Pathogen Bdellovibrio. PLoS ONE *5*, e8599.
790 https://doi.org/10.1371/journal.pone.0008599.

791 Lambert, C., Fenton, A.K., Hobley, L., and Sockett, R.E. (2011). Predatory Bdellovibrio bacteria
792 use gliding motility to scout for prey on surfaces. J Bacteriol *193*, 3139–3141.
793 https://doi.org/10.1128/JB.00224-11.

794 Lambert, C., Cadby, I.T., Till, R., Bui, N.K., Lerner, T.R., Hughes, W.S., Lee, D.J., Alderwick,
795 L.J., Vollmer, W., Sockett, R.E., et al. (2015). Ankyrin-mediated self-protection during cell
796 invasion by the bacterial predator Bdellovibrio bacteriovorus. Nat Commun *6*, 8884.
797 https://doi.org/10.1038/ncomms9884.

798 Lambert, C., Lerner, T.R., Bui, N.K., Somers, H., Aizawa, S.-I., Liddell, S., Clark, A., Vollmer,
799 W., Lovering, A.L., and Sockett, R.E. (2016). Interrupting peptidoglycan deacetylation during
800 Bdellovibrio predator-prey interaction prevents ultimate destruction of prey wall, liberating
801 bacterial-ghosts. Sci Rep *6*, 26010. https://doi.org/10.1038/srep26010.

802 Lerner, T.R., Lovering, A.L., Bui, N.K., Uchida, K., Aizawa, S.-I., Vollmer, W., and Sockett,
803 R.E. (2012). Specialized Peptidoglycan Hydrolases Sculpt the Intra-bacterial Niche of Predatory
804 Bdellovibrio and Increase Population Fitness. PLoS Pathog *8*, e1002524.
805 https://doi.org/10.1371/journal.ppat.1002524.

806 Lindeberg, T. (1998). Feature Detection with Automatic Scale Selection. International Journal of
807 Computer Vision *30*, 79–116. https://doi.org/10.1023/A:1008045108935.

808 Liu, J., Chen, C.-Y., Shiomi, D., Niki, H., and Margolin, W. (2011). Visualization of
809 bacteriophage P1 infection by cryo-electron tomography of tiny Escherichia coli. Virology *417*,
810 304–311. https://doi.org/10.1016/j.virol.2011.06.005.

811 Lyons, N.A., and Kolter, R. (2015). On the evolution of bacterial multicellularity. Current
812 Opinion in Microbiology *24*, 21–28. https://doi.org/10.1016/j.mib.2014.12.007.

813 Madhusoodanan, J. (2019). Inner Workings: Probing predatory bacteria as an antibacterial
814 remedy. Proc Natl Acad Sci USA *116*, 22887–22890. https://doi.org/10.1073/pnas.1917513116.

815 Mahmoud, K.K., and Koval, S.F. (2010). Characterization of type IV pili in the life cycle of the
816 predator bacterium Bdellovibrio. Microbiology *156*, 1040–1051.
817 https://doi.org/10.1099/mic.0.036137-0.

818 Makowski, Ł., Trojanowski, D., Till, R., Lambert, C., Lowry, R., Sockett, R.E., and Zakrzewska-
819 Czerwińska, J. (2019). Dynamics of Chromosome Replication and Its Relationship to Predatory
820 Attack Lifestyles in *Bdellovibrio bacteriovorus*. Appl Environ Microbiol *85*, e00730-19,
821 /aem/85/14/AEM.00730-19.atom. https://doi.org/10.1128/AEM.00730-19.

822 Makowski, Ł., Trojanowski, D., and Zakrzewska-Czerwińska, J. (2020). Live-Cell Imaging of
823 the Life Cycle of Bacterial Predator Bdellovibrio bacteriovorus using Time-Lapse Fluorescence
824 Microscopy. JoVE 61105. https://doi.org/10.3791/61105.

825 Martinez-Sanchez, A., Garcia, I., Asano, S., Lucic, V., and Fernandez, J.-J. (2014). Robust
826 membrane detection based on tensor voting for electron tomography. Journal of Structural
827 Biology *186*, 49–61. https://doi.org/10.1016/j.jsb.2014.02.015.

828 Mastronarde, D.N. (2005). Automated electron microscope tomography using robust prediction
829 of specimen movements. J. Struct. Biol. *152*, 36–51. https://doi.org/10.1016/j.jsb.2005.07.007.

830 Meek, R.W., Cadby, I.T., Moynihan, P.J., and Lovering, A.L. (2019). Structural basis for
831 activation of a diguanylate cyclase required for bacterial predation in Bdellovibrio. Nat Commun
832 *10*, 4086. https://doi.org/10.1038/s41467-019-12051-6.

833 Milner, D.S., Till, R., Cadby, I., Lovering, A.L., Basford, S.M., Saxon, E.B., Liddell, S.,
834 Williams, L.E., and Sockett, R.E. (2014). Ras GTPase-Like Protein MglA, a Controller of
835 Bacterial Social-Motility in Myxobacteria, Has Evolved to Control Bacterial Predation by
836 Bdellovibrio. PLoS Genet *10*, e1004253. https://doi.org/10.1371/journal.pgen.1004253.

837 Negus, D., Moore, C., Baker, M., Raghunathan, D., Tyson, J., and Sockett, R.E. (2017). Predator
838 Versus Pathogen: How Does Predatory *Bdellovibrio bacteriovorus* Interface with the Challenges
839 of Killing Gram-Negative Pathogens in a Host Setting? Annu. Rev. Microbiol. *71*, 441–457.
840 https://doi.org/10.1146/annurev-micro-090816-093618.

841 Nicastro, D. (2006). The Molecular Architecture of Axonemes Revealed by Cryoelectron
842 Tomography. Science *313*, 944–948. https://doi.org/10.1126/science.1128618.

843 Núñez, M.E., Martin, M.O., Duong, L.K., Ly, E., and Spain, E.M. (2003). Investigations into the
844 Life Cycle of the Bacterial Predator Bdellovibrio bacteriovorus 109J at an Interface by Atomic
845 Force Microscopy. Biophysical Journal *84*, 3379–3388. https://doi.org/10.1016/S0006-
846 3495(03)70061-7.

847 Oikonomou, C.M., and Jensen, G.J. (2017). A new view into prokaryotic cell biology from
848 electron cryotomography. Nature Reviews Microbiology *15*, 128.
849 https://doi.org/10.1038/nrmicro.2016.195.

850 Ortega, D.R., Yang, W., Subramanian, P., Mann, P., Kjær, A., Chen, S., Watts, K.J., Pirbadian,
851 S., Collins, D.A., Kooger, R., et al. (2020). Repurposing a chemosensory macromolecular
852 machine. Nat Commun *11*, 2041. https://doi.org/10.1038/s41467-020-15736-5.

853 Pantanella, F., Iebba, V., Mura, F., Dini, L., Totino, V., Neroni, B., Bonfiglio, G., Maria, T.,
854 Passariello, C., and Schippa, S. (2018). Behaviour of Bdellovibrio bacteriovorus in the presence
855 of Gram-positive Staphylococcus aureus. New Microbiol *41*, 145–152. .

856 Pasternak, Z., Njagi, M., Shani, Y., Chanyi, R., Rotem, O., Lurie-Weinberger, M.N., Koval, S.,
857 Pietrokovski, S., Gophna, U., and Jurkevitch, E. (2014). In and out: an analysis of epibiotic vs
858 periplasmic bacterial predators. ISME J *8*, 625–635. https://doi.org/10.1038/ismej.2013.164.

859 Pérez, J., Moraleda-Muñoz, A., Marcos-Torres, F.J., and Muñoz-Dorado, J. (2016). Bacterial
860 predation: 75 years and counting!: Bacterial predation. Environ Microbiol *18*, 766–779.
861 https://doi.org/10.1111/1462-2920.13171.

862 Pettersen, E.F., Goddard, T.D., Huang, C.C., Meng, E.C., Couch, G.S., Croll, T.I., Morris, J.H.,
863 and Ferrin, T.E. (2021a). UCSF CHIMERAX : Structure visualization for researchers, educators,
864 and developers. Protein Science *30*, 70–82. https://doi.org/10.1002/pro.3943.

865 Pettersen, E.F., Goddard, T.D., Huang, C.C., Meng, E.C., Couch, G.S., Croll, T.I., Morris, J.H.,
866 and Ferrin, T.E. (2021b). UCSF CHIMERAX : Structure visualization for researchers, educators,
867 and developers. Protein Science *30*, 70–82. https://doi.org/10.1002/pro.3943.

868 Raghunathan, D., Radford, P.M., Gell, C., Negus, D., Moore, C., Till, R., Tighe, P.J., Wheatley,
869 S.P., Martinez-Pomares, L., Sockett, R.E., et al. (2019). Engulfment, persistence and fate of
870 Bdellovibrio bacteriovorus predators inside human phagocytic cells informs their future
871 therapeutic potential. Sci Rep *9*, 4293. https://doi.org/10.1038/s41598-019-40223-3.

872 Rendulic, S. (2004). A Predator Unmasked: Life Cycle of Bdellovibrio bacteriovorus from a
873 Genomic Perspective. Science *303*, 689–692. https://doi.org/10.1126/science.1093027.

874 Rocha, B., Paul, S., and Vashisth, H. (2020). Role of Entropy in Colloidal Self-Assembly.
875 Entropy *22*, 877. https://doi.org/10.3390/e22080877.

876 Rotem, O., Pasternak, Z., and Jurkevitch, E. (2014). Bdellovibrio and Like Organisms. In The
877 Prokaryotes, E. Rosenberg, E.F. DeLong, S. Lory, E. Stackebrandt, and F. Thompson, eds.
878 (Berlin, Heidelberg: Springer Berlin Heidelberg), pp. 3–17.

879 Rotem, O., Pasternak, Z., Shimoni, E., Belausov, E., Porat, Z., Pietrokovski, S., and Jurkevitch,
880 E. (2015). Cell-cycle progress in obligate predatory bacteria is dependent upon sequential
881 sensing of prey recognition and prey quality cues. Proc Natl Acad Sci USA *112*, E6028–E6037.
882 https://doi.org/10.1073/pnas.1515749112.

883 Russo, R., Kolesnikova, I., Kim, T., Gupta, S., Pericleous, A., Kadouri, D., and Connell, N.
884 (2018). Susceptibility of Virulent Yersinia pestis Bacteria to Predator Bacteria in the Lungs of
885 Mice. Microorganisms *7*, 2. https://doi.org/10.3390/microorganisms7010002.

886 Said, N., Chatzinotas, A., and Schmidt, M. (2019). Have an Ion on It: The Life-Cycle of
887 *Bdellovibrio bacteriovorus* Viewed by Helium-Ion Microscopy. Adv. Biosys. *3*, 1800250.
888 https://doi.org/10.1002/adbi.201800250.

889 Schwudke, D., Bernhardt, A., Beck, S., Madela, K., Linscheid, M.W., Appel, B., and Strauch, E.
890 (2005). Transcriptional Activity of the Host-Interaction Locus and a Putative Pilin Gene of
891 Bdellovibrio bacteriovorus in the Predatory Life Cycle. Curr Microbiol *51*, 310–316.
892 https://doi.org/10.1007/s00284-005-0030-1.

893 Shatzkes, K., Tang, C., Singleton, E., Shukla, S., Zuena, M., Gupta, S., Dharani, S., Rinaggio, J.,
894 Connell, N.D., and Kadouri, D.E. (2017a). Effect of predatory bacteria on the gut bacterial
895 microbiota in rats. Sci Rep *7*, 43483. https://doi.org/10.1038/srep43483.

896 Shatzkes, K., Singleton, E., Tang, C., Zuena, M., Shukla, S., Gupta, S., Dharani, S., Rinaggio, J.,
897 Kadouri, D.E., and Connell, N.D. (2017b). Examining the efficacy of intravenous administration
898 of predatory bacteria in rats. Sci Rep *7*, 1864. https://doi.org/10.1038/s41598-017-02041-3.

899 Shilo, M. (1969). Morphological and Physiological Aspects of the Interaction of Bdellovibrio
900 with Host Bacteria. In Current Topics in Microbiology and Immunology, W. Arber, W. Braun, F.
901 Cramer, R. Haas, W. Henle, P.H. Hofschneider, N.K. Jerne, P. Koldovský, H. Koprowski, O.
902 Maaløe, et al., eds. (Berlin, Heidelberg: Springer Berlin Heidelberg), pp. 174–204.

903 Snellen, J.E., and Starr, M.P. (1974). Ultrastructural aspects of localized membrane damage in
904 Spirillum serpens VHL early in its association with Bdellovibrio bacteriovorus 109D. Arch
905 Microbiol *100*, 179–195. https://doi.org/10.1007/BF00446316.

906 Sockett, R.E. (2009). Predatory Lifestyle of *Bdellovibrio bacteriovorus*. Annu. Rev. Microbiol.
907 *63*, 523–539. https://doi.org/10.1146/annurev.micro.091208.073346.

908 Starr, M.P., and Baigent, N.L. (1966). Parasitic interaction of Bdellovibrio bacteriovorus with
909 other bacteria. J Bacteriol *91*, 2006–2017. https://doi.org/10.1128/JB.91.5.2006-2017.1966.

910 Stolp, H., and Starr, M.P. (1963). Bdellovibrio bacteriovorus gen. et sp. n., a predatory,
911 ectoparasitic, and bacteriolytic microorganism. Antonie van Leeuwenhoek *29*, 217–248.
912 https://doi.org/10.1007/BF02046064.

913 Stolp, H., and Starr, M.P. (1965). Bacteriolysis. Annu. Rev. Microbiol. *19*, 79–104.
914 https://doi.org/10.1146/annurev.mi.19.100165.000455.

915 Tan, J., Zhang, X., Wang, X., Xu, C., Chang, S., Wu, H., Wang, T., Liang, H., Gao, H., Zhou,
916 Y., et al. (2021). Structural basis of assembly and torque transmission of the bacterial flagellar
917 motor. Cell S009286742100430X. https://doi.org/10.1016/j.cell.2021.03.057.

918 Tang, G., Peng, L., Baldwin, P.R., Mann, D.S., Jiang, W., Rees, I., and Ludtke, S.J. (2007).
919 EMAN2: An extensible image processing suite for electron microscopy. Journal of Structural
920 Biology *157*, 38–46. https://doi.org/10.1016/j.jsb.2006.05.009.

921 Thomashow, L.S., and Rittenberg, S.C. (1985a). Waveform analysis and structure of flagella and
922 basal complexes from Bdellovibrio bacteriovorus 109J. J Bacteriol *163*, 1038–1046.
923 https://doi.org/10.1128/jb.163.3.1038-1046.1985.

924 Thomashow, L.S., and Rittenberg, S.C. (1985b). Isolation and composition of sheathed flagella
925 from Bdellovibrio bacteriovorus 109J. J Bacteriol *163*, 1047–1054.
926 https://doi.org/10.1128/jb.163.3.1047-1054.1985.

927 Thomashow, M.F., and Rittenberg, S.C. (1978a). Intraperiplasmic growth of Bdellovibrio
928 bacteriovorus 109J: solubilization of Escherichia coli peptidoglycan. J Bacteriol *135*, 998–1007.
929 https://doi.org/10.1128/JB.135.3.998-1007.1978.

930 Thomashow, M.F., and Rittenberg, S.C. (1978b). Intraperiplasmic growth of Bdellovibrio
931 bacteriovorus 109J: N-deacetylation of Escherichia coli peptidoglycan amino sugars. J Bacteriol
932 *135*, 1008–1014. https://doi.org/10.1128/jb.135.3.1008-1014.1978.

933 Thomashow, M.F., and Rittenberg, S.C. (1978c). Intraperiplasmic growth of Bdellovibrio
934 bacteriovorus 109J: attachment of long-chain fatty acids to escherichia coli peptidoglycan. J
935 Bacteriol *135*, 1015–1023. https://doi.org/10.1128/jb.135.3.1015-1023.1978.

936 Thomashow, L. S., R., S.C. (1979). Descriptive biology of the bdellovibrios. In
937 Developmental Biology of Prokaryotes. Parish, J.H. (ed.). Berkeley, CA: University of
938 California Press. 115–138. .

939 Tian, M., Wu, Z., Zhang, R., and Yuan, J. (2022). A new mode of swimming in singly
940 flagellated *Pseudomonas aeruginosa*. Proc. Natl. Acad. Sci. U.S.A. *119*, e2120508119.
941 https://doi.org/10.1073/pnas.2120508119.

942 Toyofuku, M., Nomura, N., and Eberl, L. (2019). Types and origins of bacterial membrane
943 vesicles. Nature Reviews Microbiology *17*, 13–24. https://doi.org/10.1038/s41579-018-0112-2.

944 Treuner-Lange, A., Chang, Y.-W., Glatter, T., Herfurth, M., Lindow, S., Chreifi, G., Jensen,
945 G.J., and Søgaard-Andersen, L. (2020). PilY1 and minor pilins form a complex priming the type

946 IVa pilus in Myxococcus xanthus. Nat Commun *11*, 5054. https://doi.org/10.1038/s41467-020-
947 18803-z.

948 Tudor, J.J., and Karp, M.A. (1994). Translocation of an outer membrane protein into prey
949 cytoplasmic membranes by bdellovibrios. J Bacteriol *176*, 948–952.
950 https://doi.org/10.1128/jb.176.4.948-952.1994.

951 Tudor, J.J., McCann, M.P., and Acrich, I.A. (1990). A new model for the penetration of prey
952 cells by bdellovibrios. Journal of Bacteriology *172*, 2421–2426.
953 https://doi.org/10.1128/JB.172.5.2421-2426.1990.

954 Willis, A.R., Moore, C., Mazon-Moya, M., Krokowski, S., Lambert, C., Till, R., Mostowy, S.,
955 and Sockett, R.E. (2016). Injections of Predatory Bacteria Work Alongside Host Immune Cells
956 to Treat Shigella Infection in Zebrafish Larvae. Current Biology *26*, 3343–3351.
957 https://doi.org/10.1016/j.cub.2016.09.067.

958 Yamaguchi, T., Makino, F., Miyata, T., Minamino, T., Kato, T., and Namba, K. (2020).
959 Structure of the molecular bushing of the bacterial flagellar motor (Molecular Biology).

960 Zheng, S.Q., Keszthelyi, B., Branlund, E., Lyle, J.M., Braunfeld, M.B., Sedat, J.W., and Agard,
961 D.A. (2007). UCSF tomography: an integrated software suite for real-time electron microscopic
962 tomographic data collection, alignment, and reconstruction. J. Struct. Biol. *157*, 138–147.
963 https://doi.org/10.1016/j.jsb.2006.06.005.

964 Zhu, S., and Gao, B. (2020). Bacterial Flagella Loss under Starvation. Trends in Microbiology
965 https://doi.org/10.1016/j.tim.2020.05.002.

966 Zhu, S., Schniederberend, M., Zhitnitsky, D., Jain, R., Galán, J.E., Kazmierczak, B.I., and Liu, J.
967 (2019). *In Situ* Structures of Polar and Lateral Flagella Revealed by Cryo-Electron Tomography.
968 Journal of Bacteriology *201*. https://doi.org/10.1128/JB.00117-19.

969 Zhuang, X.-Y., and Lo, C.-J. (2020). Construction and Loss of Bacterial Flagellar Filaments.
970 Biomolecules *10*, 1528. https://doi.org/10.3390/biom10111528.

971 Zhuang, X., Guo, S., Li, Z., Zhao, Z., Kojima, S., Homma, M., Wang, P., Lo, C., and Bai, F.
972 (2020). Live-cell fluorescence imaging reveals dynamic production and loss of bacterial flagella.
973 Molecular Microbiology *114*, 279–291. https://doi.org/10.1111/mmi.14511.

974 Zivanov, J., Nakane, T., Forsberg, B.O., Kimanius, D., Hagen, W.J., Lindahl, E., and Scheres,
975 S.H. (2018). New tools for automated high-resolution cryo-EM structure determination in
976 RELION-3. ELife *7*, e42166. https://doi.org/10.7554/eLife.42166.

977

978 # Figure legends

979 **Figure 1: Anatomy of attack-phase *B. bacteriovorus*. A)** A slice through an electron cryo-
980 tomogram of an attack phase *B. bacteriovorus* cell, with enlarged views of the flagellated (red)
981 and biting (blue) poles. White rectangles highlight the flagellar motor (upper panel) and non-
982 piliated T4aP basal body (lower panel), and the white ellipse highlights a rose-like complex.
983 Question mark points to a cross-section through a periplasmic tubular structure, and white arrow
984 to a type IVa pilus. Scale bars are 50 nm. **B-D)** Central slices through subtomogram averages of
985 the *B. bacteriovorus* flagellar motor (B), rose-like complex (C), and non-piliated T4aP basal body
986 (D). White arrows in D point to the extracellular ring of the T4aP basal body. Scale bars are 20
987 nm. Dashed black lines indicate a composite of slices through the tomogram at different z-heights
988 in (A), and a composite of subtomogram averages aligned on the outer and inner membrane,
989 respectively, in (C). OM = outer membrane, IM = inner membrane.
990
991 **Figure 2: Attachment of *B. bacteriovorus* to prey. A)** A slice through an electron cryo-tomogram
992 showing a *B. bacteriovorus* cell attached to a prey (*E. coli* minicell) vi a T4aP. OM = outer
993 membrane, IM = inner membrane. **B)** A Slice through an electron cryo-tomogram of *B.*
994 *bacteriovorus* attached to prey (*E. coli* minicell) showing non-piliated T4aP basal bodies (white
995 ellipses) penetrating to the prey's PG layer. **C)** A slice through an electron cryo-tomogram of *B.*
996 *bacteriovorus* attached to prey with a polar attachment plaque. PG = peptidoglycan. Scale bars 100
997 nm.
998
999 **Figure 3: *B. bacteriovorus* flagellar absorption. A)** A slice through an electron cryo-tomogram
1000 showing a *B. bacteriovorus* cell attached to a prey via an attachment plaque with its flagellum

resorbing into the periplasm. Enlargements in the red-boxed areas highlight different parts of the absorbed flagellum. Scale bar is 50 nm in the main panel, 20 nm in the enlargements. **B)** A 3D segmentation of panel (A) and an enlarged view illustrating different parts of the absorbed flagellum.

Figure 4: *B. bacteriovorus* prey invasion. A) A slice through an electron cryo-tomogram (left) and enlarged view (right) showing a stalled invasion by a *B. bacteriovorus* of an *E. coli* minicell. Blue arrows and inset schematic highlight the portal. **B)** Right (top): Cross-section through the *yz* plane of the tomogram shown in (A) along the black dotted line indicated on the left. Note that this slice does not include the portal. Right (bottom): Average density profile taken along the white dashed line (inside the white rectangle) in the top panel. The distance between the predator's inner (IM) and outer membranes (OM) is indicated (20 nm). **C)** Similar to (B) but for a *yz* slice where the portal is visible. The distance between the predator's inner and outer membranes is indicated (10 nm). The schematics in the right panels of (A-C) represent the white-boxed areas in the corresponding slices, with the portal shown in blue, the prey outer membrane in grey, and the predator inner and outer membranes in black. Scale bars 100 nm in the left panel of (A), and 50 nm in other panels.

Figure 5: Anatomy of the bdelloplast. A-C) Slices (at different z-levels) through an electron cryo-tomogram of a *V. cholerae* bdelloplast containing two *B. bacteriovorus* after predator division. **D)** A 3D segmentation of the bdelloplast shown in (A-C). **E)** Enlargement (left) and 3D segmentation (right) of the white-boxed area in (A), highlighting the features of the seal. **F)** Enlargement (left) and 3D segmentation (right) of the white-boxed area in (C), rotated 180°,

highlighting the prey flagellar relic. OM= outer membrane. Scale bars 100 nm in (A-C) and 50 nm in (E, F).

Figure 6: Ribosomal nucleoid lattice in the end-stage bdelloplast. A, B) Slices (at different z-levels) through an electron cryo-tomogram of an end-stage *E. coli* bdelloplast containing two *B. bacteriovorus* cells after predator division, highlighting the hexagonal arrangement of ribosomes around the nucleoids. **C, D)** Rotated views of a 3D segmentation of the nucleoids and ribosomes of the cryo-tomogram shown in (A, B). Scale bars 50 nm. **E)** Distances of individual ribosomes from the nucleoid surface measured in the 3D segmentations of the cryo-tomogram shown in (A&B) ("experiment," solid line), compared to a simulation of randomly distributed 20 nm-wide spheres packed in the same segmented volume ("random," dashed line). See also Movie S16.

Acknowledgements

This project was funded by the National Institutes of Health (grant R01 AI127401 to G.J.J) and a Baxter postdoctoral fellowship from Caltech to M.K. S.K. is supported by the Swedish Research Council (2019-06293). Cryo-ET work was performed in the Beckman Institute Resource Center for Transmission Electron Microscopy at the California Institute of Technology and the Howard Hughes Medical Institute Janelia Farm CryoEM Facility. We thank Daniel Villanueva Avalos for making the summary animation. We are deeply grateful to Prof. Liz Sockett (University of Nottingham) for the gift of the *B. bacteriovorus* strain and helpful advice and comments.

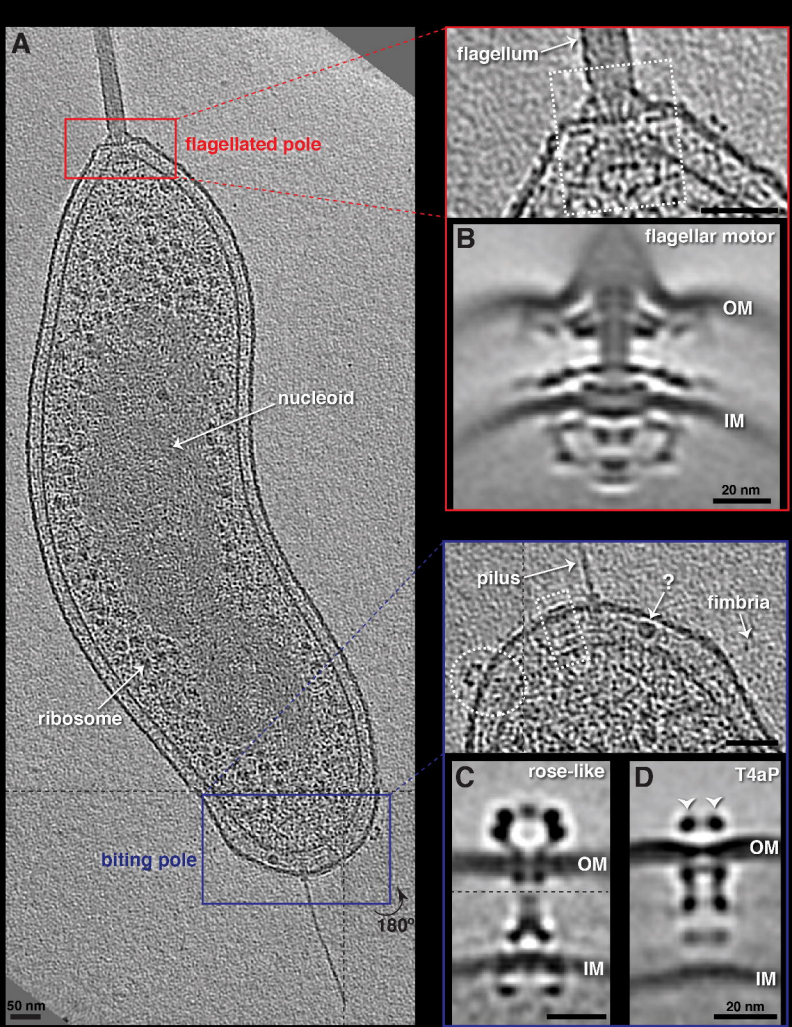
A
flagellated pole
flagellum
B
flagellar motor
OM
IM
20 nm
nucleoid
ribosome
biting pole
180°
50 nm
pilus
?
fimbria
C
rose-like
OM
IM
D
T4aP
OM
IM
20 nm

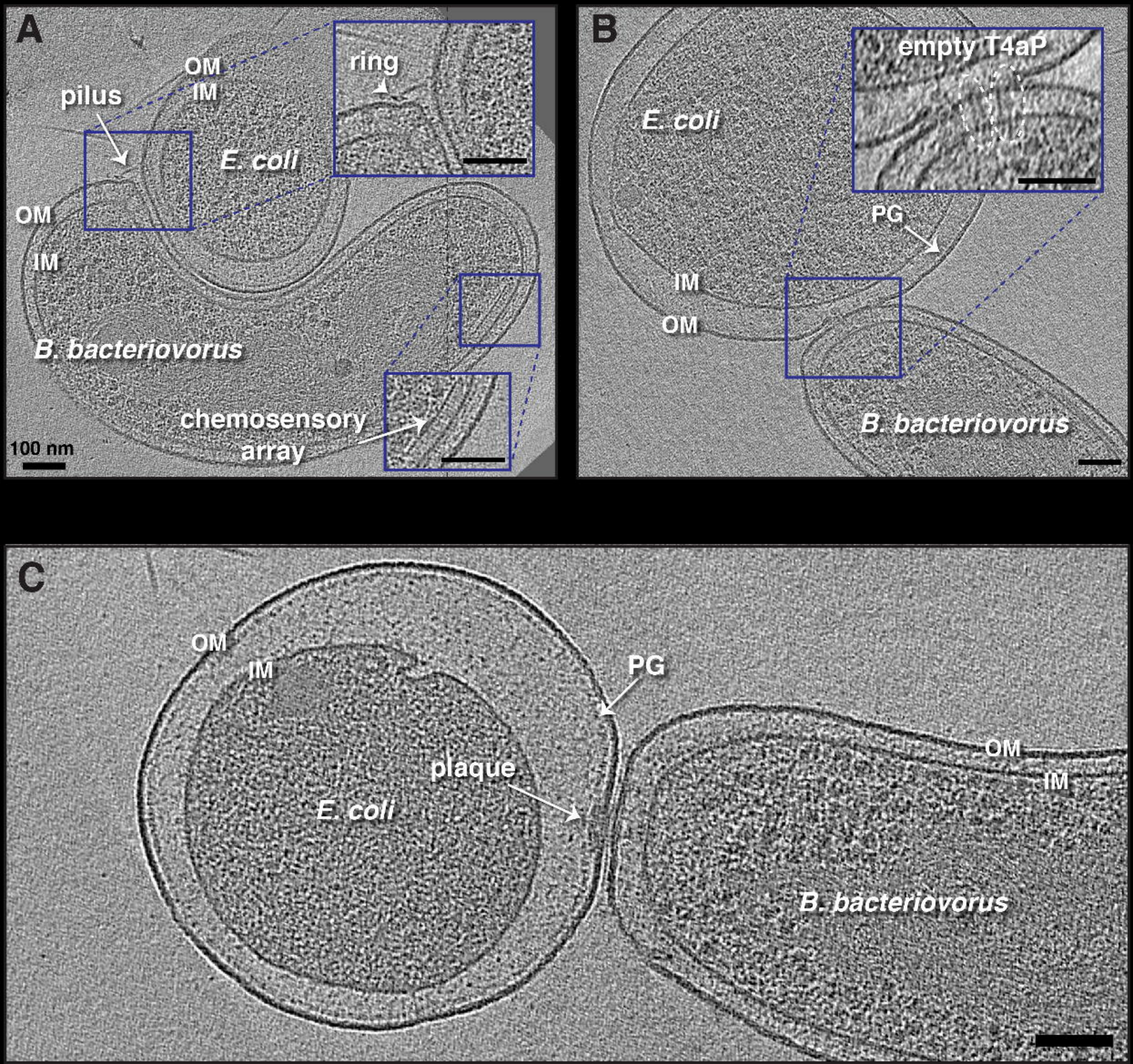
A
OM
IM
pilus
ring
E. coli
OM
IM
B. bacteriovorus
chemosensory
array
100 nm
B
empty T4aP
E. coli
PG
IM
OM
B. bacteriovorus
C
OM
IM
PG
plaque
E. coli
OM
IM
B. bacteriovorus

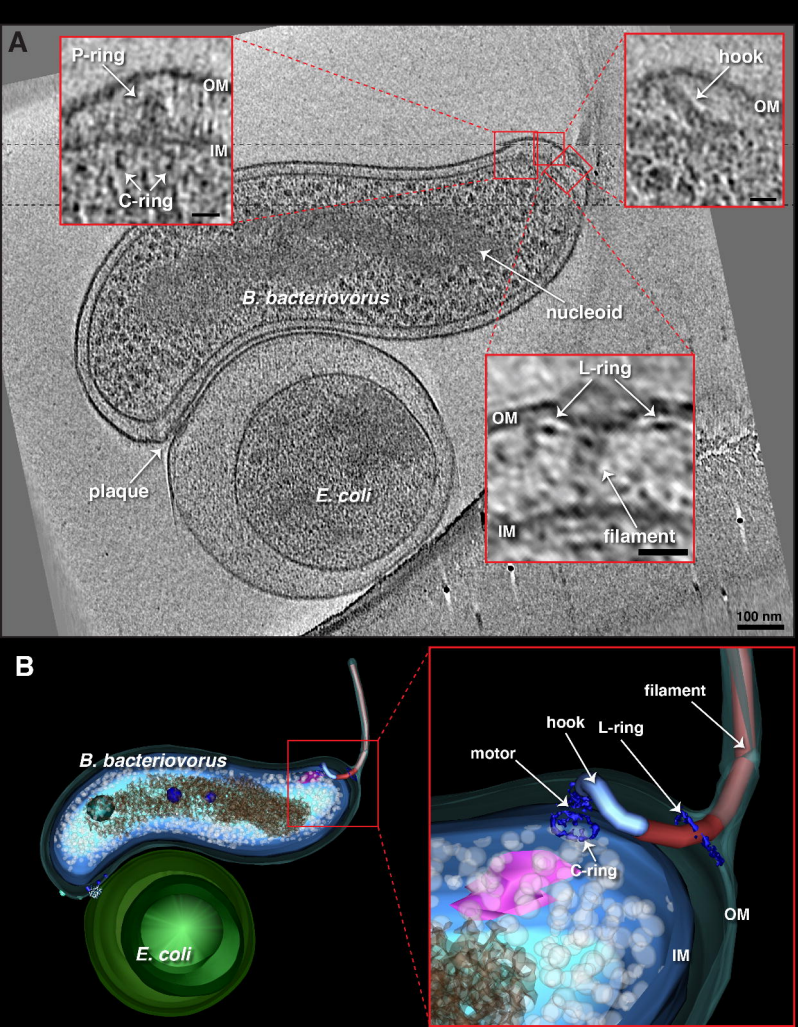
A
P-ring
OM
IM
C-ring
hook
OM
B. bacteriovorus
nucleoid
L-ring
OM
IM
filament
plaque
E. coli
100 nm
B
B. bacteriovorus
E. coli
filament
hook
L-ring
motor
C-ring
OM
IM

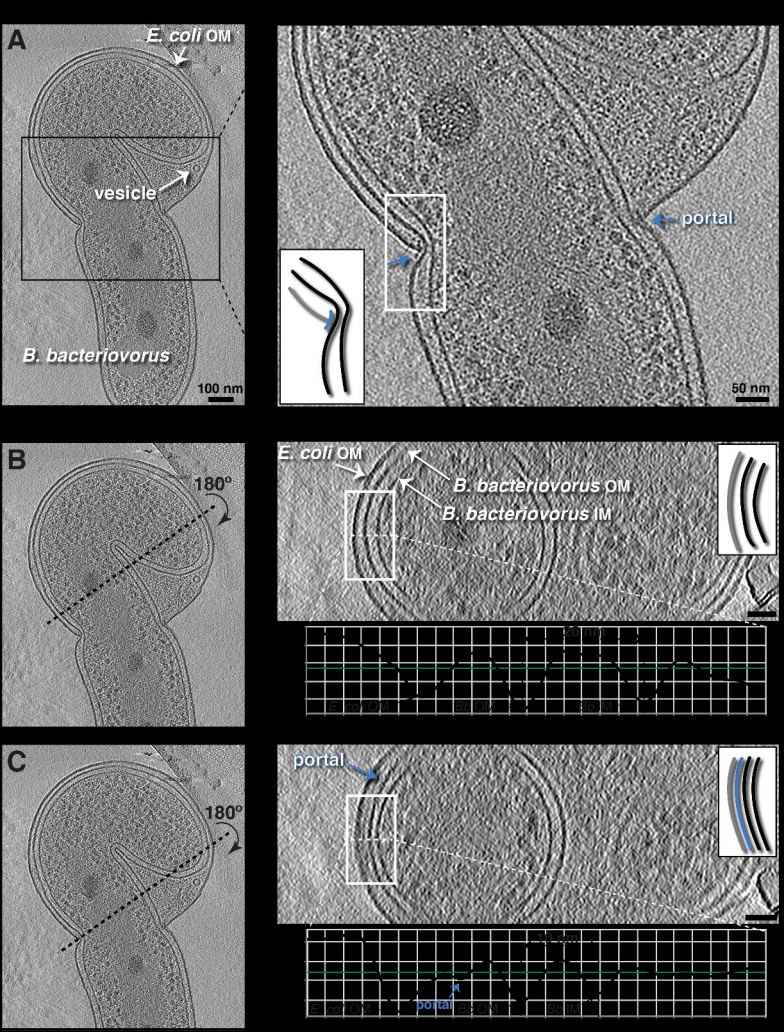
A
E. coli OM
vesicle
B. bacteriovorus
100 nm
portal
50 nm
B
180°
E. coli OM
B. bacteriovorus OM
B. bacteriovorus IM
C
180°
portal
portal

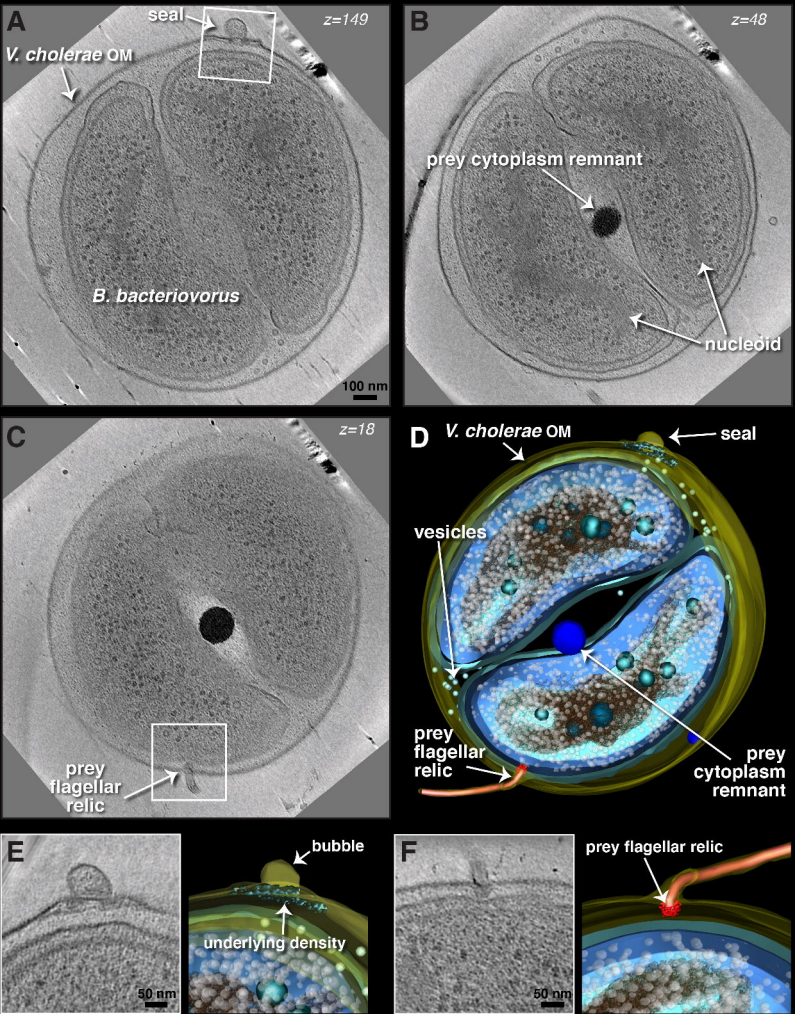
A
seal
z=149
V. cholerae OM
B. bacteriovorus
100 nm
B
z=48
prey cytoplasm remnant
nucleoid
C
z=18
prey flagellar relic
D
V. cholerae OM
seal
vesicles
prey flagellar relic
prey cytoplasm remnant
E
bubble
underlying density
50 nm
F
prey flagellar relic
50 nm

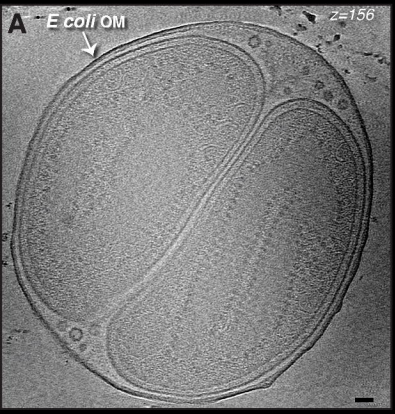
A
E coli OM
z=156

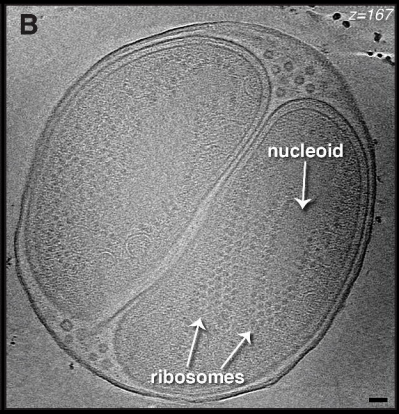
B
z=167
nucleoid
ribosomes

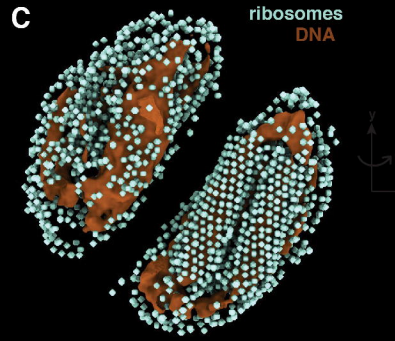
C
ribosomes
DNA
y
180°
x

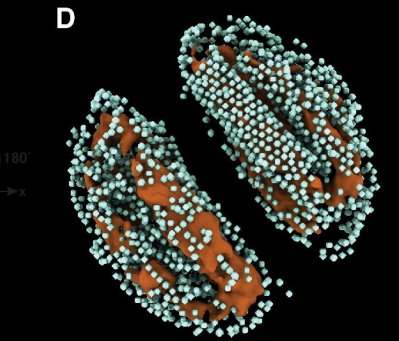
D

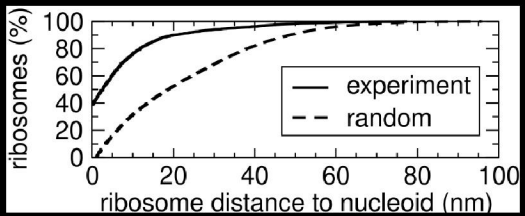
E
ribosomes (%)
100
80
60
40
20
0
0
20
40
60
80
100
experiment
random
ribosome distance to nucleoid (nm)